atmosphere

MDPI

Article

Multiscale Dynamics Organizing Heavy Precipitation During Tropical Cyclone Hilary's (2023) Remnant Passage over the Southwestern U.S.

Jackson T. Wiles [1,2,*], Michael L. Kaplan [3] and Yuh-Lang Lin [1,2]

[1] Department of Physics, North Carolina A&T State University, Greensboro, NC 27411, USA; ylin@ncat.edu
[2] Applied Science & Technology Ph.D. Program, North Carolina A&T State University, Greensboro, NC 27411, USA
[3] Division of Atmospheric Sciences, Desert Research Institute, Reno, NV 89512, USA; michael.kaplan@dri.edu
* Correspondence: jtwiles@ncat.edu

Abstract

The Weather Research and Forecasting Model (WRF-ARW) version 4.5 was used to simulate the synoptic to mesoscale evolving atmosphere of Tropical Cyclone (TC) Hilary's (2023) remnant passage over the southwestern United States. The atmospheric dynamic processes conducive to the precursor rain events were extensively studied to determine the effects of mid-level jetogenesis. Concurrently, the dynamics of mesoscale processes related to the interaction of TC Hilary over the complex topography of the western United States were studied with several sensitivity simulations on a nested 2 km × 2 km grid. The differential surface heating between the cloudy California coast and clear/elevated Great Basin plateau had a profound impact on the lower-mid-tropospheric mass field resulting in mid-level jetogenesis. Diagnostic analyses of the ageostrophic flow support the importance of both isallobaric and inertial advective forcing of the mid-level jetogenesis in response to differential surface sensible heating. This ageostrophic mesoscale jet ultimately transported tropical moisture in multiple plumes more than 1000 km poleward beyond the location of the extratropical transition of the storm, resulting in anomalous flooding precipitation within a massive arid western plateau.

Keywords: Tropical Cyclone Hilary (2023); mid-level jet; ageostrophic wind diagnostics; complex terrain; numerical modeling; Weather Research and Forecasting (WRF) Model; Advanced Research WRF core (WRF-ARW)

Academic Editor: Yubin Li

Received: 11 December 2025
Revised: 12 January 2026
Accepted: 13 January 2026
Published: 14 January 2026

1. Introduction

Tropical Cyclone (TC) Hilary's (2023) southwestern U.S. landfall led to an extraordinary and rare inland rainfall event over the Great Basin. This manuscript will explore the multiscale dynamics that organized this unique and complex inland precipitation event. Tropical storms rarely make landfall in the southwest U.S. However, when they do, the potential for anomalous orographic rainfall does exist. For example, TC Hilary formed on 16 August and began its west-northwestward track resulting from the strong steering of the massive mid-level ridge dominating the southwestern United States and northern Mexico. Hilary rapidly intensified to major hurricane status by 17 August due to optimal environmental conditions in the Pacific and aloft. Hilary eventually made landfall near

Baja California (CA) as a weakened tropical storm at 1700 UTC 20 August due to less favorable atmospheric conditions and cooler SSTs. Hilary quickly dissipated into a disorganized tropical low with moisture and precipitation occurring primarily poleward of the storm center. The remnants of Hilary were then absorbed by a deep-layer trough located off the coast of CA, and the declassification of Hilary from tropical to post-tropical occurred at 2100 UTC 20 August [1].

During Hilary's landfall, low-level extratropical dynamics began to reflect the warm-season complex terrain forcing. Consistent with the moist environment Hilary transported along the Baja and CA coasts, a shallow, cloudy, and cool marine air boundary layer formed, extending into southwestern AZ and equatorward to northern Baja CA. Because of this marine planetary boundary layer (PBL), coastal land locations cooled due to a lack of surface sensible heating and evaporational cooling from rainfall. This shallow marine PBL propagated beyond the coastal locations, providing a sharp gradient to the well-mixed PBL inland with clear skies downstream over interior CA, Arizona (AZ), Nevada (NV), and Utah (UT). Because of clear skies, August sun angle, and elevation mostly > 1.5 km, the interior Great Basin PBL is very deep, extending above 3 km mean sea level, and is very hot and dry. This results in a well-defined southeast-northwest temperature boundary forced by an orthogonal (southwest to northeast) heating gradient which develops between the inland elevated desert of the Great Basin to the east and north and the coastal regions to the southwest. The focus of this manuscript is to analyze the following dynamical/thermodynamical processes: Hilary's cloud shield effect, combined with multiple massive mountain-plain solenoids over the Great Basin, created a mass adjustment which resulted in mid-level jetogenesis adjusting to the terrain-forcing heating asymmetry. Poleward moisture transport and lift, resulting from the mid-upper-level velocity divergence, both caused by this mid-level poleward-directed jet organized significant rainfall accompanying mesoscale convective systems (MCSs) over the arid regions of interior southern CA, NV, and UT.

2. Literature Review

Several sub-synoptic circulations organized the unique rainfall event in the Great Basin after Hilary's landfall, and in this section, we will describe some of the pertinent literature on those circulations.

2.1. Mass Circulation and Ageostrophic Processes

Wolf and Johnson [2] explored the relationship between mass circulation and ageostrophic processes with an idealized three-dimensional simulated convective system (SCS), by using isentropic diagnostics. The two main objectives of this study were to (1) identify the mesoscale adiabatic/diabatic processes' interaction within the SCS to static/inertial instabilities and (2) properly identify the role of latent heat release in isallobaric ageostrophic motion and inertial ageostrophic adjustment (see Equation (1)). Results clearly depict the importance of isallobaric and inertial advective ageostrophic forcing in generating convective outflow downstream.

$$\mathbf{U_{ag}} = \frac{\mathbf{1}}{\boldsymbol{f}}\widehat{\boldsymbol{k}} \times \left(\frac{\boldsymbol{\partial}}{\boldsymbol{\partial t_\theta}} + \mathbf{U} \cdot \boldsymbol{\nabla_\theta} + \dot{\boldsymbol{\theta}}\frac{\boldsymbol{\partial}}{\boldsymbol{\partial \theta}}\right)\mathbf{U_g} \quad (1)$$

2.2. Mountain-Plain Solenoids and Mesoscale Convective Systems

In the complex terrain of southwestern North America, the mountain-plain solenoid (MPS) circulation becomes important due to the role of surface differential heating. During the daytime, rising motion over the upward slopes of mountains can create a slope pressure deficit as air parcels rise due to surface sensible heating. As a result, the upper

https://doi.org/10.3390/atmos17010082

return branch of the MPS is generated over complex topography and a descending branch over the plains. At night, the circulation reverses.

MPS circulations are known to initiate convection. Bao and Zhang [3] conducted a study on the impacts of the MPS circulation and cold pool dynamics over northern China. Sun and Zhang [4] investigated the influence of MPS circulations on daily precipitation and mesoscale convective vortices associated with the Mei-Yu front in coastal Asia. Hua et al. [5] showed that MPS circulations during the daytime over complex topography enhanced low-level convergence and in the precursor environment, nocturnal gravity waves developed over complex topography due to a stable PBL. From the plateau-scale MPS, a quasi-linear convective system (QLCS) formed and brought an abundance of rainfall between the Taiyue Mountains and the Changzhi Basin due to strong low-level convergence. In contrast to Sun and Zhang, the LLJ was not present and the primary source of precipitation came from orographic effects [4]. The removal of the topography significantly affected the development of the QLCS and accumulated precipitation, demonstrating the importance of the MPS circulation over mountains. Tripoli and Cotton [6] described a conceptual model showing the genesis of MCSs developing over complex topography. In their conceptual model, the direct MPS circulation becomes indirect as convection weakens and the ageostrophic circulation drives vertical motion instead. Carbone and Tuttle [7] also mention the importance of nocturnal reversals of MPS circulations over the plains, which lead to significant rainfall.

In addition to inducing convective initiation, MPS circulations can directly impact the formation of mesoscale jet streaks. In the Cooperative Convective Precipitation Experiment (CCOPE) field experiment, a mesoscale jet streak was observed (11–12 July 1981), resulting in numerical simulations which described the formation mechanisms, dynamics, and impacts of gravity waves through geostrophic and associated mass adjustments [8]. In Zhang and Koch's study [9], a continuation and expansion of Kaplan et al.'s case study was given [8], showing the underlying mechanisms behind the genesis and evolution of gravity waves. It was found that dynamic interactions of a propagating density current against mountains highly influenced the generation of gravity waves.

2.3. Climatology of Landfalling Tropical Cyclones in the Southwestern U.S.

The western U.S. experiences significantly fewer TCs than the Gulf of Mexico and the eastern seaboard. Corbosiero et al. [10] explored the contributions of Eastern North Pacific (ENP) TCs to the average rainfall in the southwestern U.S. and validated the rarity of these events [10]. Within the 46-year study period of 1958–2003, only 35 TCs impacted the southwestern U.S., which corresponds to roughly 6–10% of all ENP storms. Additionally, the rainfall contributions of these TCs contributed ~10–15% of the regional rainfall average, except higher amounts locally over complex topography. Furthermore, Dominguez and Magaña [11] explored how seasonal precipitation was modulated from TCs across the tropical eastern Pacific and found that in extreme cases from 1979–2013, TCs brought up to 40–60% of the annual precipitation. From Ritchie et al.'s [12] findings, landfalling TC remnants transport a significant amount of tropical moisture and can lead to widespread flooding/heavy precipitation events. When TC remnants interact with topography, considerable precipitation may occur. In this research, 43 Eastern North Pacific TCs were examined, spanning from 1992 to 2005, and it was found that 81% brought precipitation to the U.S. with some accounting for up to 30% of the annual precipitation. On average, approximately three TC circulations affect the southwestern U.S. each year, primarily during August–October. For the TC remnant events that did not directly produce any U.S. rainfall, the cloud shield effect extended well inland and inhibited normal monsoonal MCSs through less surface radiative heating. As a result of their study, four unique categories

were identified for how TCs in the ENP may traverse, found in Figure 1 with their corresponding TC examples.

In our research, TC Hilary likely fits into their Group III, but has specific implications for annual precipitation due to the unusually strong mid-level jetogenesis approximately 1000 km ahead of the landfalling TC and disassociated with the remnant upper-level outflow circulation. Ritchie et al.'s analyses did not examine circulations organizing rainfall over the southwestern U.S. and Mexico (dynamics and thermodynamics) [12]. In our research we will address the underlying thermodynamics and dynamics driving the relatively large amount of precipitation accumulated in the southwestern U.S./Great Basin region from this TC event.

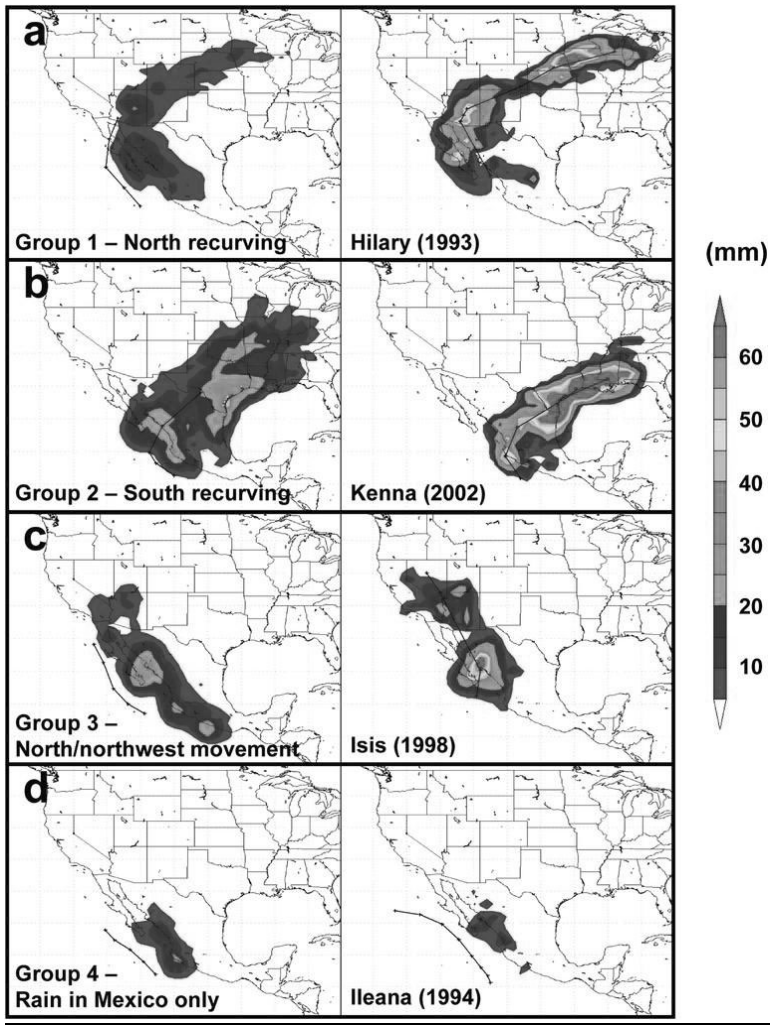

Figure 1. Eastern North Pacific TC group climatology and corresponding TC examples representative of each group. Shading represents the average rainfall swath given in mm. Group 1 (**a**) = north recurving track—Hilary (1993); Group 2 (**b**) = south recurving track—Kenna (2002); Group 3 (**c**) = north-northwest track—Isis (1998); Group 4 (**d**) = no U.S. rainfall track—Ileana (1994) [12].

Galarneau et al. [13] explored 28 predecessor rain events (PREs) occurring ~1000 km ahead of landfalling TCs in the eastern U.S. within the period 1995–2008. Cote defined PREs as coherent areas of significant rainfall rates (≥100 mm within 24 h) which are separate from the rain shield region of the TC while the moisture transport is from the TC itself [14]. In most cases, PREs would occur up to 36 h before the TC's rain bands enter the region. Galarneau et al. found that PREs are most frequent in August–September and approximately 30% of TCs produce at least one PRE. Of the 28 events studied, 17 were

associated with an anticyclonically curved upper-level jet, which is similar to the ridge of high pressure over the U.S. during Hilary's passage [13].

Regarding TC Hilary, diabatic heating accompanying differential surface sensible heat fluxes above the elevated terrain was crucial for downstream jetogenesis. Additionally, the suppression of heating by the incoming cloud shield primed the environment for ageostrophic motion, comprising the mid-level jet. Changes in the slope of the PBL isentropic surfaces from the southwest/coastal region to the northeast/inland region allowed for ageostrophic motions causing the rapid ascent of air parcels to enter the mid-level jet. Therefore, the mid-level jet subsequently organized the precursor MCSs/subsequent inland precipitation because of the poleward transport of moisture and accompanying ascent downstream of Hilary making landfall.

3. Numerical Model Description and Experimental Design

We used the Weather Research and Forecasting model's (WRF) Advanced Research WRF (WRF-ARW) version 4.5. The European Centre for Medium Range Weather Forecasts (ECMWF) ERA5 dataset was utilized to initialize WRF-ARW and provide the lateral boundary conditions on an hourly basis [15]. The domain configuration for this study is shown in Figure 2. To simulate the synoptic-meso-α-scale patterns for the organization of TC Hilary, domain 1 (D01) was created. To study phenomena on the meso-β scale, primarily over land, a nested domain (D02) is included and covers the southwestern U.S. D01 was initialized six days prior to TC Hilary's formation. D02 was initialized ~36 h prior to mid-level jetogenesis over the Great Basin as well as the landfall time of TC Hilary in Baja CA. Table 1 below indicates the start and end dates for D01 and D02 as well as the physical parameterizations employed. For a detailed description of the physical parameterizations used, please refer to the WRF-ARW user manual [16]. The physical parameterizations were based on Agyakwah and Lin's study on Typhoon Morakot (2009). In their study, significant terrain-induced convection occurred, leading to orographic precipitation. Additionally, their CTRL simulation was validated against the observed track, intensity proxies from the Japan Meteorological Agency, rainfall structures, and rainfall totals. Therefore, due to the similarities between terrain-induced precipitation and circulations and the associated tropical environment, a similar approach was taken. In addition to the control simulation (CTRL), three additional sensitivity simulations were performed. The first was the smooth terrain (ST) simulation which increased the smoothing routine of the HGT variable in the WRF-ARW Preprocessing System (WPS). The purpose was to smooth the terrain to render elevated surface sensible heating gradients relative to the planetary boundary layer in the nearby atmosphere irrelevant. In the second sensitivity experiment, heat and moisture fluxes over land were set to zero without varying for the entire simulation (NHMFL) while in the third simulation, surface heat and moisture fluxes were turned off over the entire grid (NHMFLO). This was completed by modifying the surface physics, surface layer physics, and the land surface model codes to correctly identify land and manually set the heat and moisture fluxes to zero. Primarily, the NCAR Command Language version 6.6.2 plotting software was used [17] while ageostrophic analyses utilized Python version 3.11.14.

Table 1. WPS domain specifics, parameterizations, and schemes used for WRF-ARW simulations.

WPS Domain Configuration Specifics	
D01 Start–End Dates	0000 UTC 10 August–0000 UTC 23 August 2023
D01 Resolution and Grid Points	10 km × 10 km (492 × 488)
D02 Start–End Dates	0000 UTC 19 August–1200 UTC 22 August 2023
D02 Resolution and Grid Points	2 km × 2 km (951 × 851)
Parameterizations and Schemes Used	
Microphysics	Goddard 4-Ice Scheme
Longwave Radiation	RRTM Longwave
Shortwave Radiation	Dudhia shortwave
Surface Layer Physics	Revised MM5 Monin–Obukhov
Land Surface Physics	Unified Noah Land-Surface Model
Surface Urban Physics	None
Planetary Boundary Layer Physics	YSU
Cumulus Physics (D01 only)	Kain–Fritsch (new Eta)

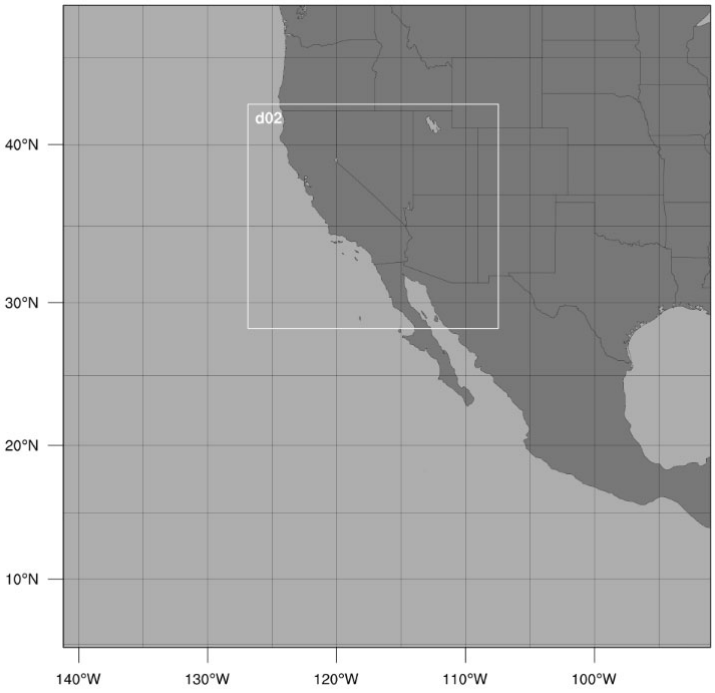

Figure 2. WPS domain configurations for parent domain (D01) and nest (D02) for running WRF-ARW version 4.5.

4. Observational and Simulated Analyses

4.1. Observational Analyses

The average annual precipitation varies extensively over the western U.S. due in large part to complex terrain (Figure 3). Little moisture is typically found over the inland arid regions of the Great Basin, resulting in minimal rainfall yearly except for an active but rare summer monsoon season. The focal point of this study is shown in the zoomed-in region of Figure 3. The majority of southern CA and south-central NV receive less than eight inches (in. or ~200 mm) of precipitation annually, while most of the Great Basin region, spanning NV through the western half of UT, receives 8 to 12 in. (~200–300 mm) of precipitation, with greater amounts over the higher mountains. In rare cases where landfalling TCs are

present, tropical moisture can be transported into arid regions and can be coupled with other circulations to generate substantial rainfall, as was the case for TC Hilary.

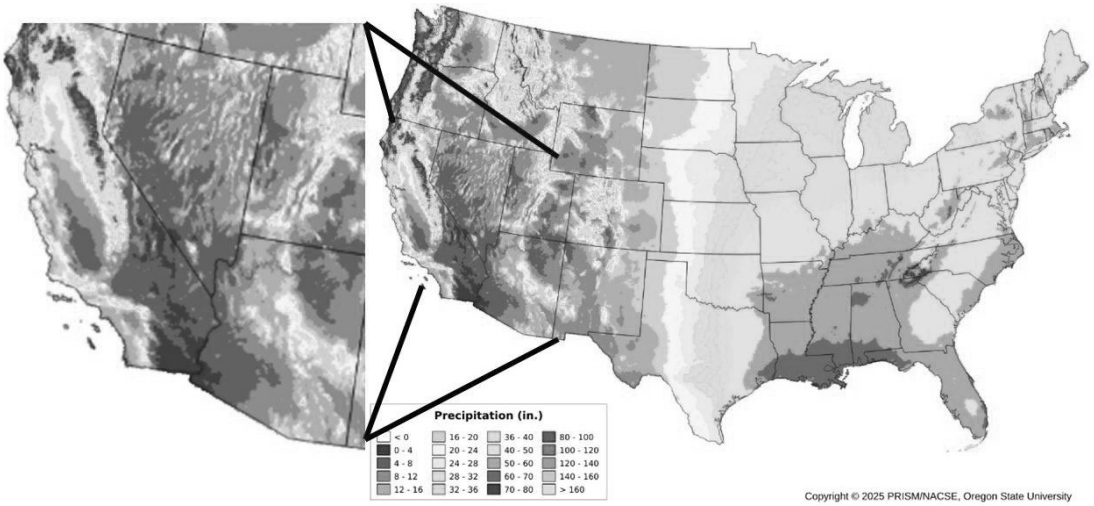

Figure 3. Thirty–year normal average annual precipitation for the U.S. from 1991–2020 with a focus on the southwestern U.S. [18].

Figure 4 depicts accumulated precipitation from 19–21 August 2023, stemming from TC Hilary. The San Gabriel, San Bernardino, and San Jacinto Mountains in southern CA received approximately 10–13 in. (254–330 mm) of rain, roughly 30% of their annual total, while one to five in. (~25–127 mm) fell poleward through NV. Additional pockets of one to three in. (~25–76 mm) fell near Reno, NV, and in south-central UT. Comparing the average annual precipitation totals to Figure 4 shows that most of the region received between 25–50% of their annual rainfall in <1% of the year.

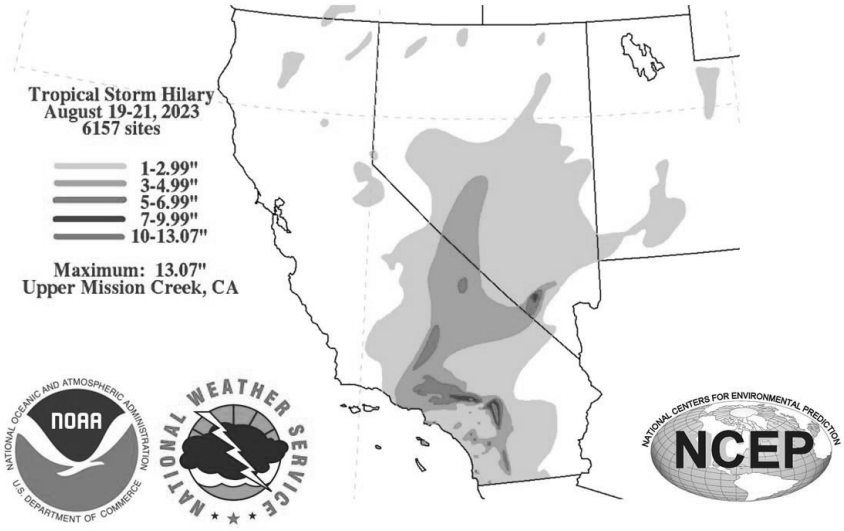

Figure 4. TC Hilary (2023) accumulated precipitation in inches for the period 19–21 August 2023 [1].

Figure 5 depicts the hourly precipitation maximum of 1.30 in. (~33 mm), 0.80 in. (~20 mm), and 1.40 in. (~36 mm) for (a) Reno, NV (KGRX), (b) Salt Lake City, UT (KMTX), and (c) Cedar City, UT (KICX), respectively. To further distinguish between the landfalling TC and these precipitation rate maxima, notice the timing of precipitation maxima compared to the coastal locations. These radar-derived precipitation rates occur approximately 8–17

h prior to the landfall of Hilary in Baja CA, which is, at that time, ~1500–2400 km poleward of the center of circulation. This indicates the presence of MCSs in the region due to the tropical moisture transport preceding Hilary. For geographical and station locations, please refer to Appendix A, Figure A2.

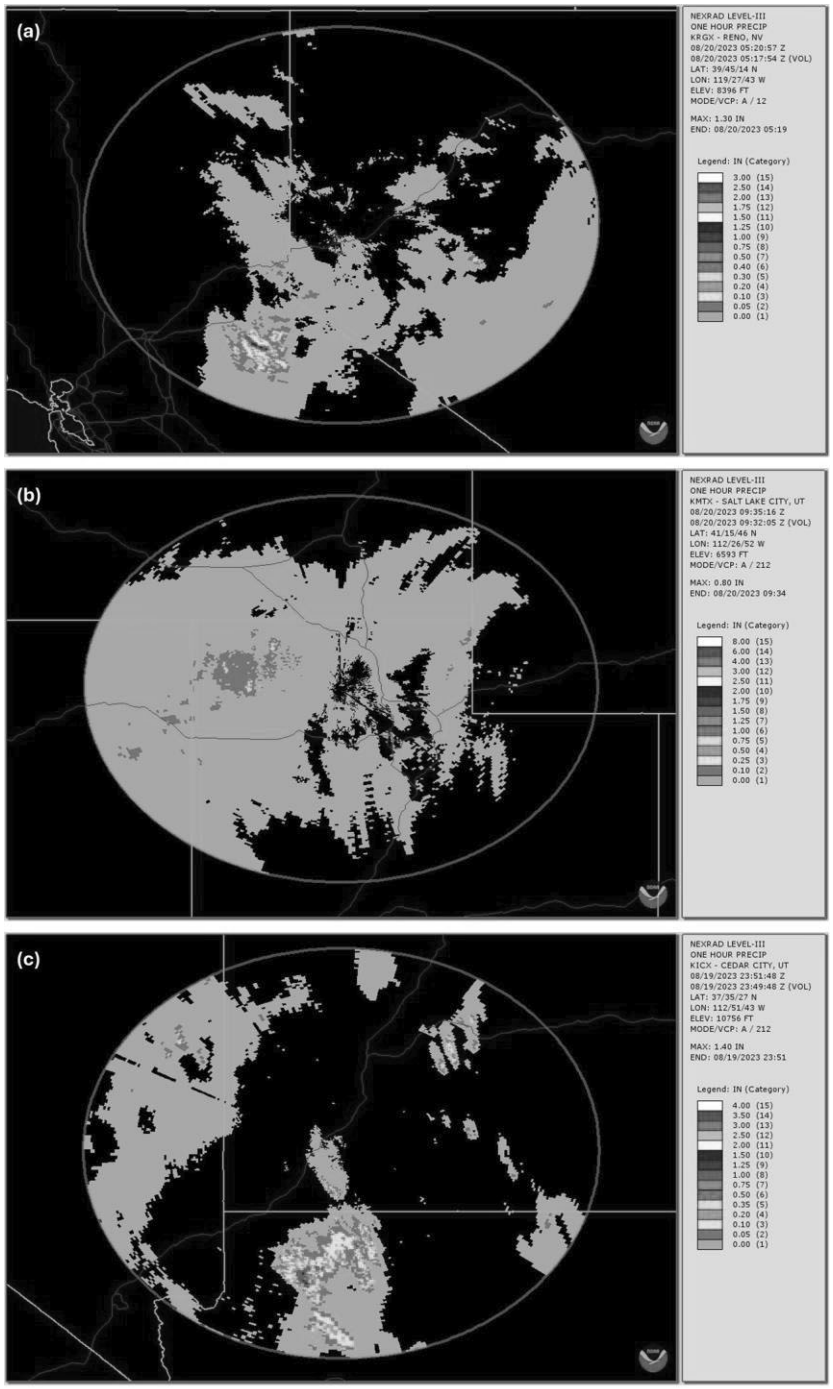

Figure 5. NOAA NCEI NEXRAD hourly precipitation rate maximums for KGRX (Reno, NV) (**a**), KMTX (Salt Lake City, UT) (**b**) and KICX (Cedar City, UT) (**c**), showing maxima of 1.30 in. (33 mm), 0.80 in. (~20 mm), and 1.40 in. (~36 mm), respectively [19].

The 500 hPa heights in Figure 6a,b indicate a massive westward-extending mid-level ridge of high pressure over the central U.S. directing anticyclonic flow poleward over the southwestern U.S. The mid-level jet is embedded within the western periphery of this ridge, representing a sub-synoptic wind maximum. Over western AZ, the mid-level jet begins forming on 0000 UTC 20 August and rapidly expands poleward within 12 h. The

hatched region of ≥40 knots (KT or ~21 ms^{-1}), in Figure 6a,b, rapidly intensifies to 60 KT (~31 ms^{-1}) over portions of southern CA, western AZ, and eastern NV along with a wind shift from southeast to south. In addition, a plume of warm air flanks the jet, represented by the red isotherms, in the lower troposphere primarily above the elevated Great Basin Plateau extending poleward from western Arizona–western Utah and eastern Nevada (Figure 7b).

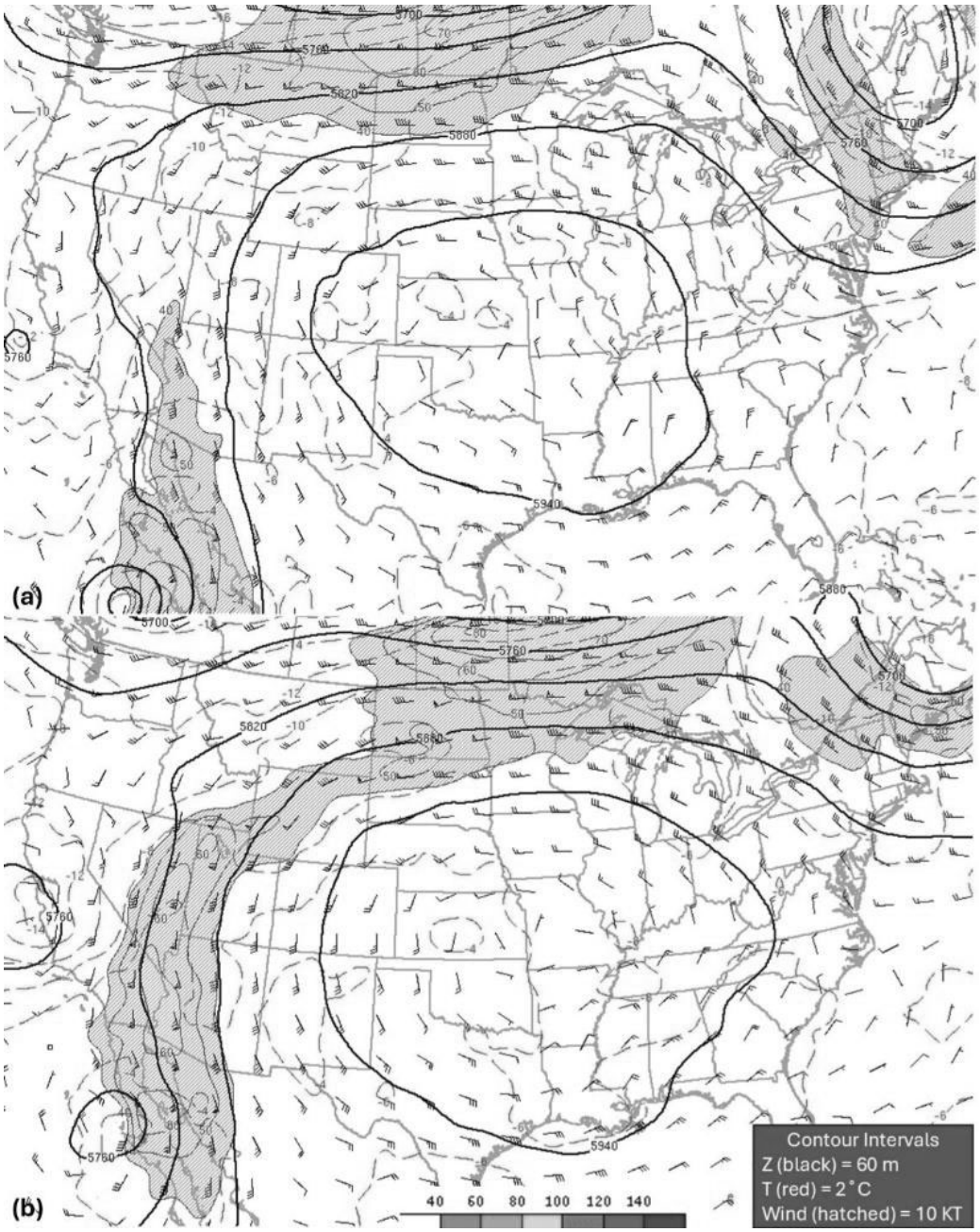

Figure 6. NOAA SPC 500 hPa height (m MSL, black), temp. (degrees C, blue/red) and wind (KT, hatched ≥ 40 KT or ~21 ms^{-1}). Panel (**a**) represents 0000 UTC 20 August, and panel (**b**) represents 1200 UTC 20 August [20].

Figure 7a,b show the 0000–1200 UTC 20 August 700 hPa heights, wind, mean 700–500 hPa relative humidity (RH) and temperature fields. Most notably, the mean RH correlates well with the mid-level jet location. In addition, the low-level temperature gradient between Arizona, Nevada and Utah is more pronounced than at earlier times and is even more significant downward through the near-surface layer at ~850 hPa. This is influenced by the differential shortwave radiative forcing resulting from the surface

heating of the eastern Great Basin in clear air and the developing cloud shield of TC Hilary extending into southern California and western Nevada. Therefore, with clear skies over the desert region, the incoming shortwave radiation will heat the surface more effectively with negligible reflection from cloud cover. Further exploration of the cloud shield effect and surface heating will be discussed in the simulation result section.

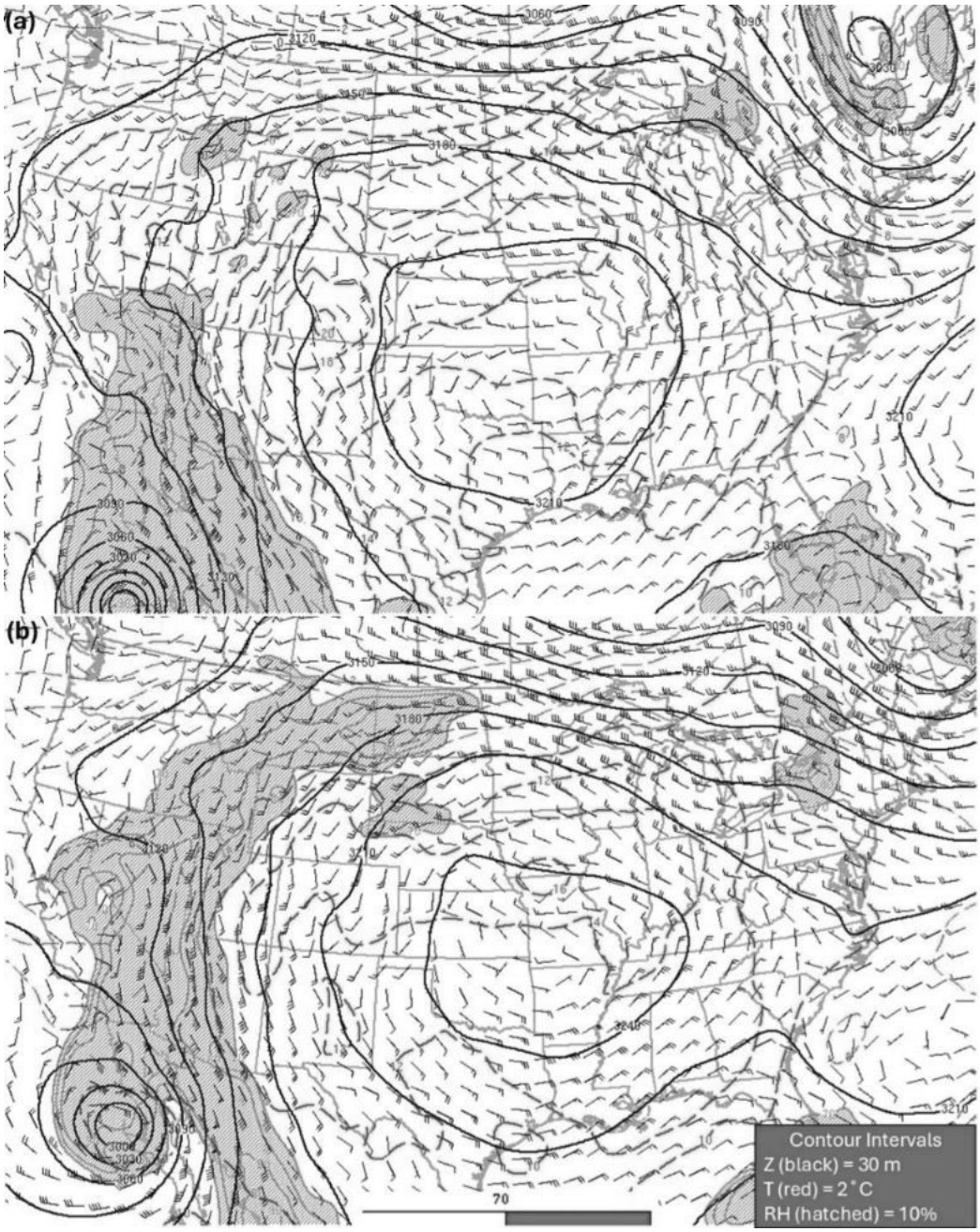

Figure 7. NOAA SPC 700 hPa height (m MSL, black), temp. (degree C, blue/red), wind (KT) and 700–500 hPa mean RH ≥ 70%. Panel (**a**) represents 0000 UTC 20 August, and panel (**b**) represents 1200 UTC 20 August [20].

Figure 8 represents moisture flux convergence (MFC) and the 100 hPa mean mixing ratio. Valid on 0000 UTC 20 August, Figure 8a shows that the mean mixing ratio is negligible for central and northern NV while a line of demarcation can be seen in southern NV, indicating the extent of tropical moisture. Negative MFC is found over southern NV, indicating that the mid-level jet has not formed or extended into the region because there exists little moisture advection. By 1200 UTC 20 August (Figure 8b), higher values of the

mean mixing ratio have extended poleward through NV and a clear area of MFC can be seen in central NV. This area of positive MFC collocates well with the mid-level jet and demonstrates that the newly formed mid-level jet is transporting tropical moisture poleward, allowing convection in the form of MCSs.

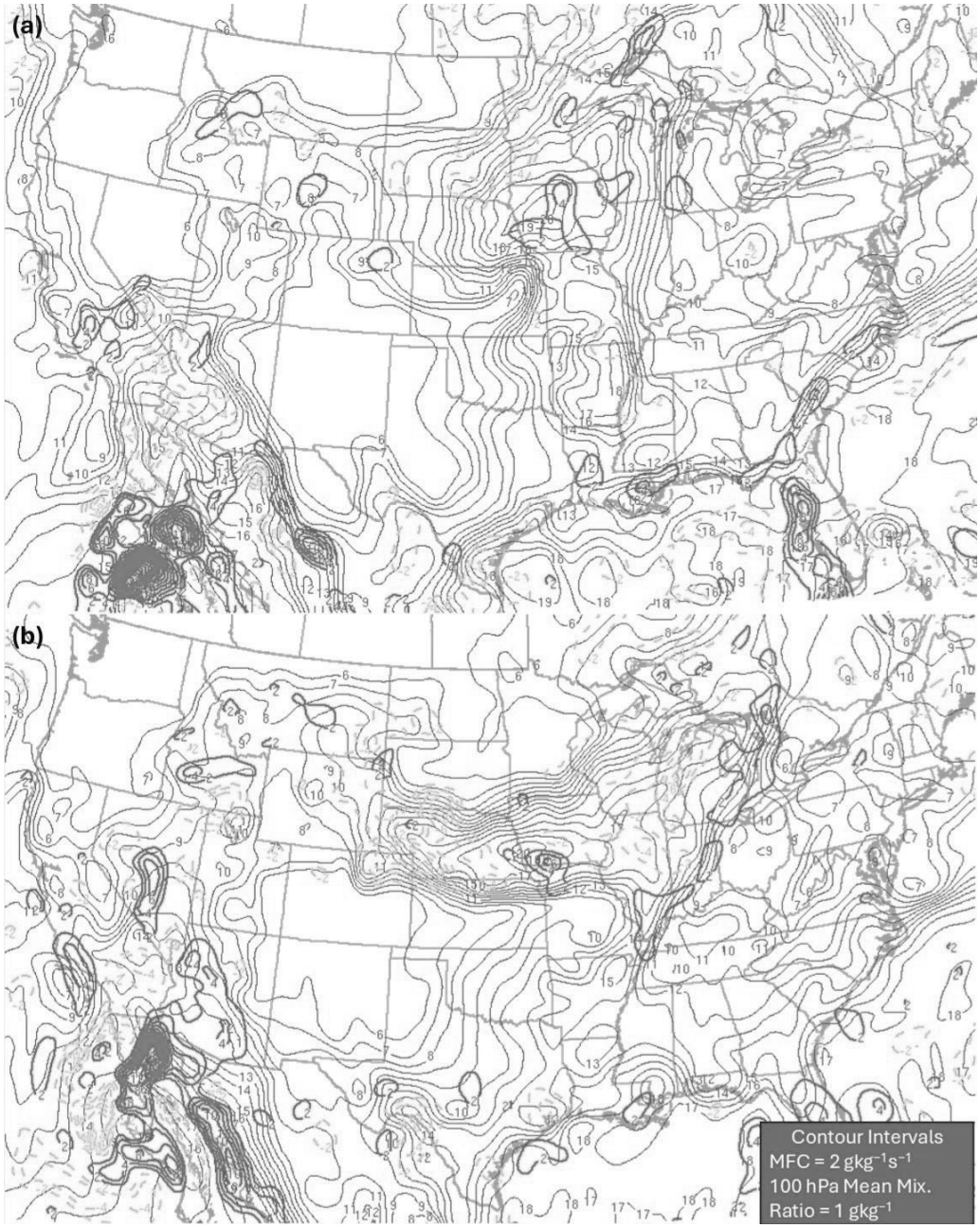

Figure 8. NOAA SPC moisture flux convergence (MFC) (red contours = positive; cyan contours = negative), and 100 hPa mean mixing ratio (green contours). Panel (**a**) represents 0000 UTC 20 August, and panel (**b**) represents 1200 UTC 20 August [20].

Figure 9 depicts observational soundings for Las Vegas, NV (VEF), valid at 0600 UTC (9a), 1200 UTC (9b), and 1800 UTC (9c) on 20 August 2023. In Figure 9a, wind speed increases with height, but has a northeasterly component near the surface before veering sharply to a southerly flow aloft. In Figure 9b, the mid-level jet becomes visible as it strengthens and propagates over VEF. The southerly wind velocity increases vertically from approximately 800 hPa to 600 hPa before decreasing above 600 hPa. This distinguishes the upper-level jet from the mid-level jet, as above 275 hPa, another maximum

exists. However, in Figure 9c, the mid-level jet has merged with the outflow of TC Hilary propagating over land.

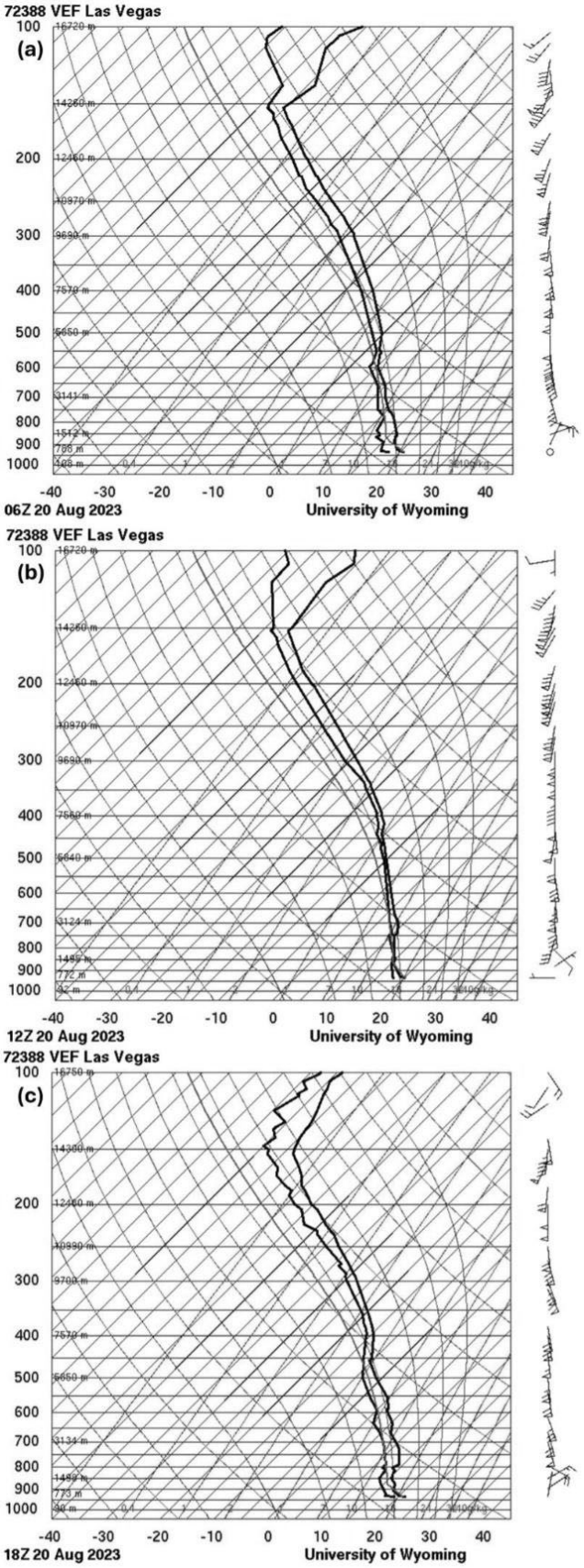

Figure 9. Observed soundings from Las Vegas, NV (VEF), valid at 0600 UTC (**a**), 1200 UTC (**b**), and 1800 UTC (**c**) on 20 August 2023 [21].

Figure 10, at 1200 UTC 20 August, depicts several MCSs in the radar reflectivity. Most notably, two separate MCSs are present near Las Vegas, NV (i.e., one poleward and another equatorward as indicated by the core reflectivity values of ~40 dBZ). As these MCSs propagate through the region, significant rainfall occurs which is physically separate from the TC Hilary circulation. Additionally, MCSs are located over Fresno, CA, north-central NV, and northwestern UT. Due to the mid-level jet, the environment is conducive for MCSs to form as it facilitates the advection of tropical moisture > 1000 km poleward of the TC remnants. This is consistent with the VEF soundings in Figure 9 which depict deep layers of near-saturation conditions and moist neutrality. Analysis of the mid-level jet and a validation of the simulation will be shown in the following section.

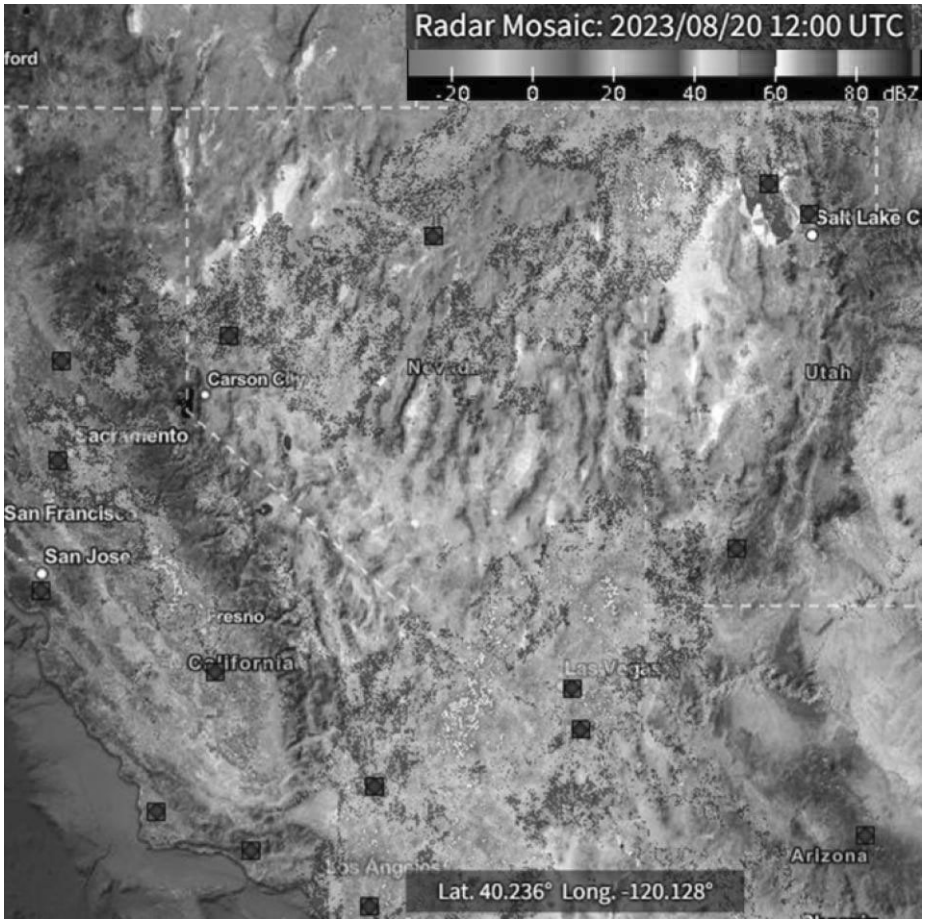

Figure 10. NOAA NCEI NEXRAD radar reflectivity analysis valid 1200 UTC 20 August 2023. Notice placement of MCSs over central and southern CA, north-central NV and Las Vegas, NV [19].

4.2. Simulated Analyses

Figure 11 shows the simulated WRF-ARW reflectivity valid at 1200 UTC 20 August. Representative MCSs over north-central CA, north-central NV, and Las Vegas, NV, into southern CA are shown in the simulation. When compared to Figure 10 observations, the MCS over Las Vegas, NV, and in nearby CA are represented well in terms of location, time, and intensity, i.e., ~45 dBZ. Additionally, in northern NV, broader MCSs with similar reflectivity values are shown, consistent with observations and in proximity to the mid-level jet.

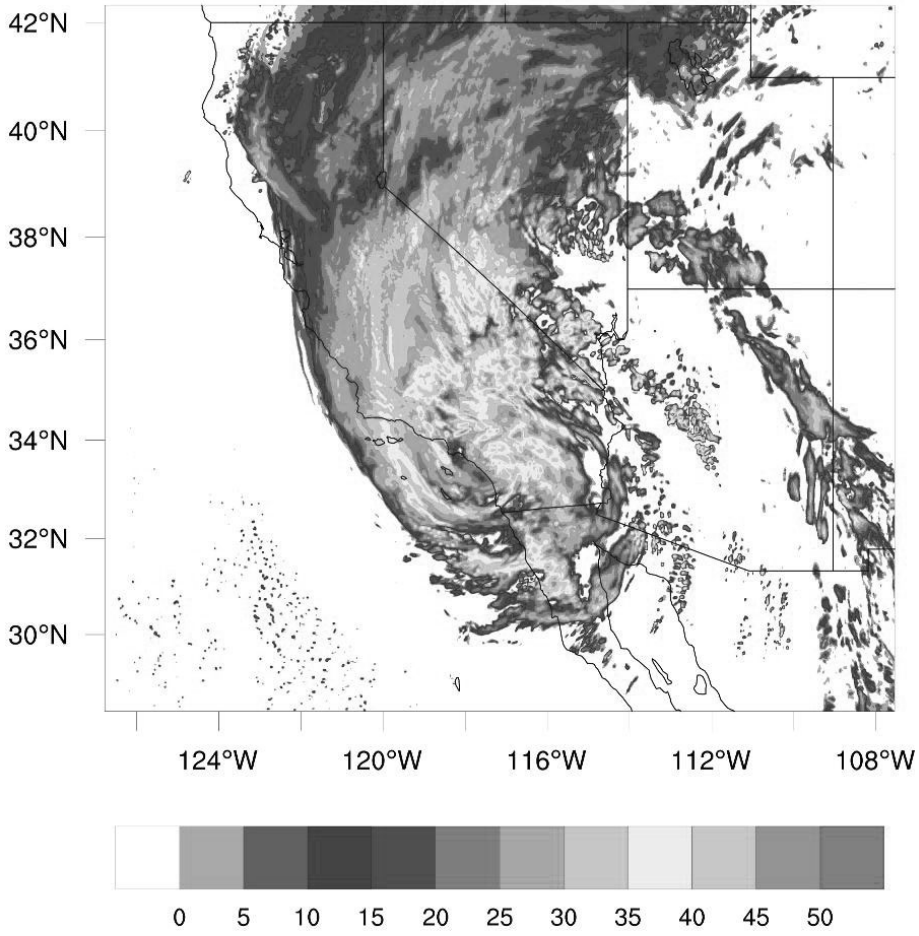

Figure 11. D02 WRF-ARW simulated reflectivity (dBZ) valid at 1200 UTC 20 August 20.

Surface heating in the lower Great Basin region of southwestern UT and eastern NV significantly impacts the formation of the mid-level jet. Figure 12 investigates the thermodynamics and wind speed/direction through the low (700 hPa) and mid levels (600 hPa) of the troposphere, valid at 0600 UTC 20 August. Note the larger-scale inverted trough over northern CA and its associated cold pool. This cold pool creates a broad temperature gradient from western CA to western UT, ~12 degrees C/400 km at 600 hPa. The wind profile at 600 hPa indicates a south-southeasterly flow near Las Vegas, NV, while the flow turns more southerly poleward. Shown in Figure 12b (700 hPa), the initiation of the mid-level jet appears near Las Vegas, NV, in proximity to the 10-degree C/100 km gradient extending from central to eastern NV. Furthermore, with the winds increasing in intensity above 700 hPa to 600 hPa, a separate circulation exists in the mid levels. However, in the NHMFL simulation (Figure 12c) at 600 hPa, the alignment of the cold pool in northern CA extends further east into northwestern NV. As a result, the pre-existing temperature gradient over central NV becomes less evident. Due to the lack of heat and moisture fluxes over land, the wind speed decreases from ~ 30 ms^{-1} to 15 ms^{-1}. Figure 12d shows even weaker winds with a more uniform distribution of temperature over the central U.S. When the heat and moisture fluxes are eliminated over land and ocean (simulation NHMFLO, Figure 12e,f), a completely different synoptic/sub-synoptic simulated atmosphere exists with sub-synoptic fictitious circulations, the lack of TC Hilary, as well as a nonexistent mid-level jet. In Figure 12g,h, in the ST simulation, wind speeds increase across the continental U.S. because of less friction from the complex topography, allowing for less restricted passage of the TC remnant circulation/expansion. The significant temperature gradient still exists over central NV in Figure 12h. However, due to the smooth terrain, the mid-level jet has no time to form before the expansion of

the TC remnant circulation as it moves poleward. Therefore, no distinction between the mid-level and outflow jet from the TC circulation can be made, which is inconsistent with the observations.

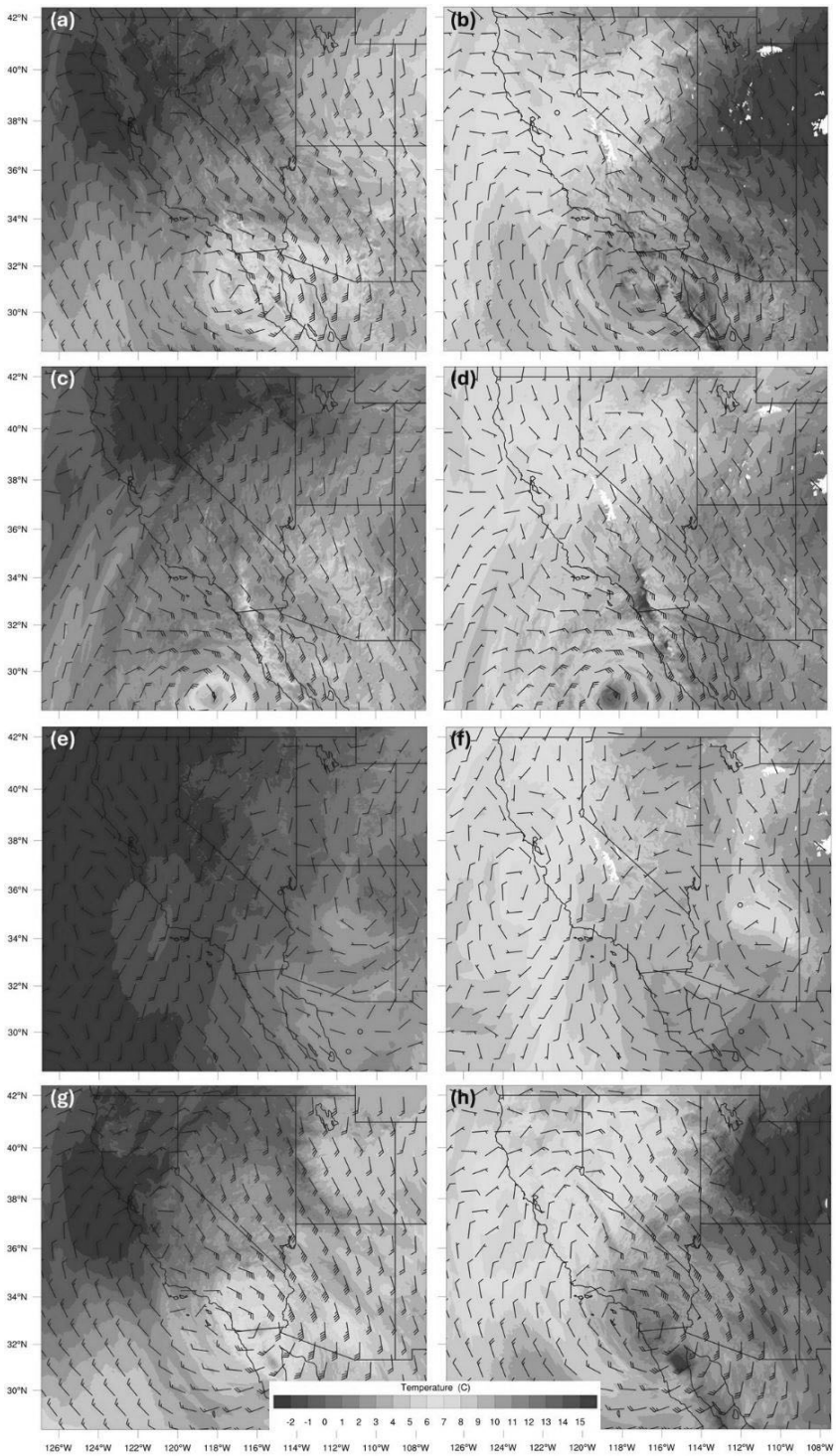

Figure 12. D02 WRF-ARW simulated temperature (degree C in color) and wind barbs (ms^{-1}) valid at 0600 UTC 20 August 2023. CTRL simulation = panels (**a**,**b**). NHMFL simulation = panels (**c**,**d**). NHMFLO = panels (**e**,**f**). ST = panels (**g**,**h**). Panels (**a**,**c**,**e**,**g**) = 600 hPa surface. Panels (**b**,**d**,**f**,**h**) = 700 hPa.

Significant mid-level jet moisture transport can be found in the mid to lower levels of the troposphere. Figure 13 shows the corresponding water vapor mixing ratio (Qv) for the same time, 0600 UTC 20 August, for 600 hPa and 700 hPa as well as wind barbs discussed in Figure 12. Comparing Figure 13a–d (CTRL vs. NHMFL simulation) shows how

primarily the heat and moisture fluxes affect the Qv concentration over the Great Basin. Along the southern NV and CA border, a decrease in wind speed and lack of Qv are evident. However, at the 700 hPa level, Figure 13b shows a more significant concentration of Qv over central and southern NV, collocating well with the maximum temperature gradient in Figure 12b. However, the NHMFL simulation in Figure 13d shows an anomalous concentration of Qv over central and southern NV with slower wind velocities. This anomalous Qv concentration is attributable to the weak, dry frontal confluence zone diagonally located in the Bay Region of northern CA and extending southwestward deep into the Pacific Ocean, which forces Qv convergence. Figure 13e,f show a drastically different spread of Qv compared to the CTRL (Figure 13a,b). With the lack of heat and moisture fluxes over land and ocean (NHMFLO), incoming tropical moisture is negligible while pre-existing moisture over UT and AZ. is unchanged. In the ST simulation (Figure 13g,h), Qv magnitudes change minimally within the 600–700 hPa layer, but because of less terrain impact in this simulation, the Qv envelope slightly expands.

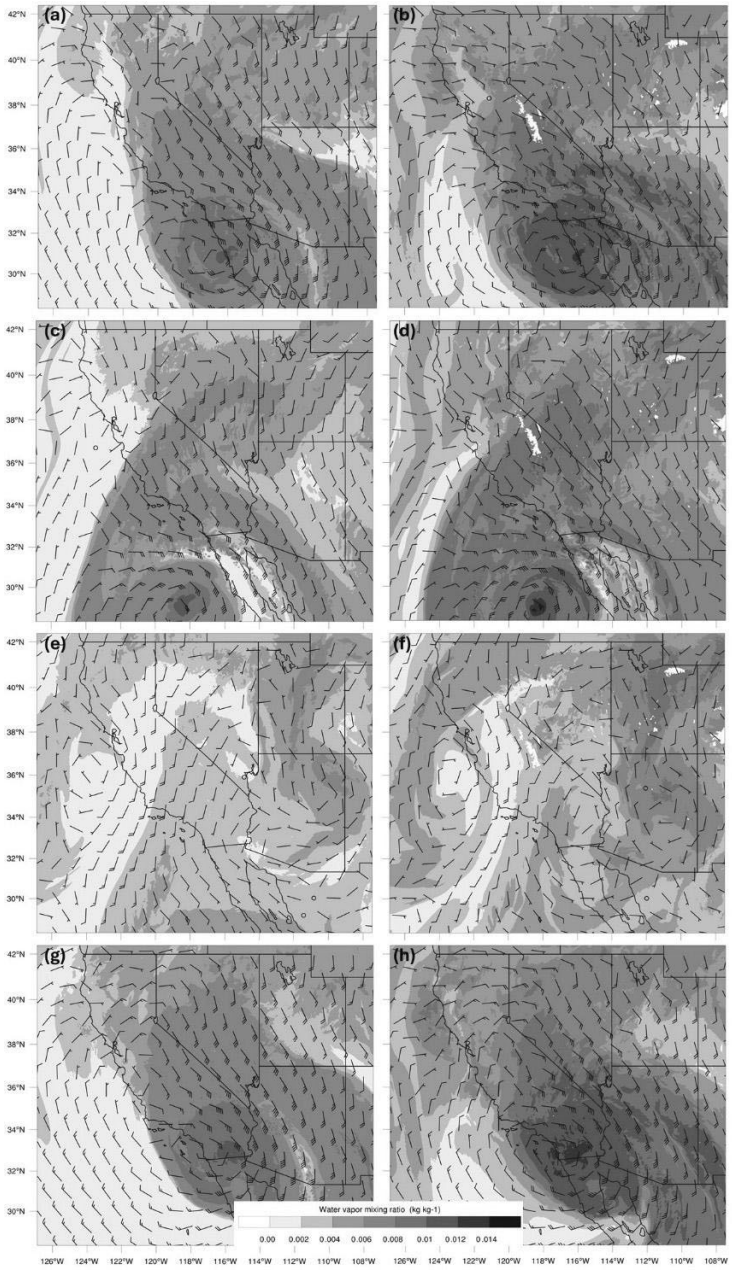

Figure 13. D02 WRF-ARW simulated water vapor mixing ratio ($kgkg^{-1}$ in color) and wind barbs (ms^{-1}) valid at 0600 UTC 20 August 2023. CTRL simulation = panels (**a**,**b**). NHMFL simulation =

panels (**c**,**d**). NHMFLO = panels (**e**,**f**). ST = panels (**g**,**h**). Panels (**a**,**c**,**e**,**g**) = 600 hPa surface. Panels (**b**,**d**,**f**,**h**) = 700 hPa surface.

From the accumulated rainfall analysis (Figure 14a), it is evident that the CTRL case gives an adequate representation of the amount of rainfall and the spread of values compared to observations (Figure 4) for the period 2100 UTC 19 August to 2100 UTC 20 August. However, in the NHMFL simulation (Figure 14b), a significant decrease in rainfall exists due to the lack of MCSs caused by lower-mid tropospheric mass and moisture flux diffluence over land resulting from the absence of the mid-level jet. Therefore, it is evident that an important interaction exists between surface heat fluxes and the rainfall associated with the MCSs or the lack thereof along the boundary of the maximum temperature gradient. In the NHMFLO simulation (Figure 14c), without the tropical moisture being advected into the region, no significant rainfall can occur, demonstrating the importance of heat and moisture fluxes over land and ocean to inland precipitation. For the ST simulation (Figure 14d), an overall decrease in precipitation among local mountainous regions exists due to the lower terrain heights even though the spread of Qv extends wider than the CTRL. Without the orographic lifting effects on air parcels, less rainfall is simulated. For ASOS/METAR station analyses of accumulated precipitation, please refer to Appendix A, Figure A1.

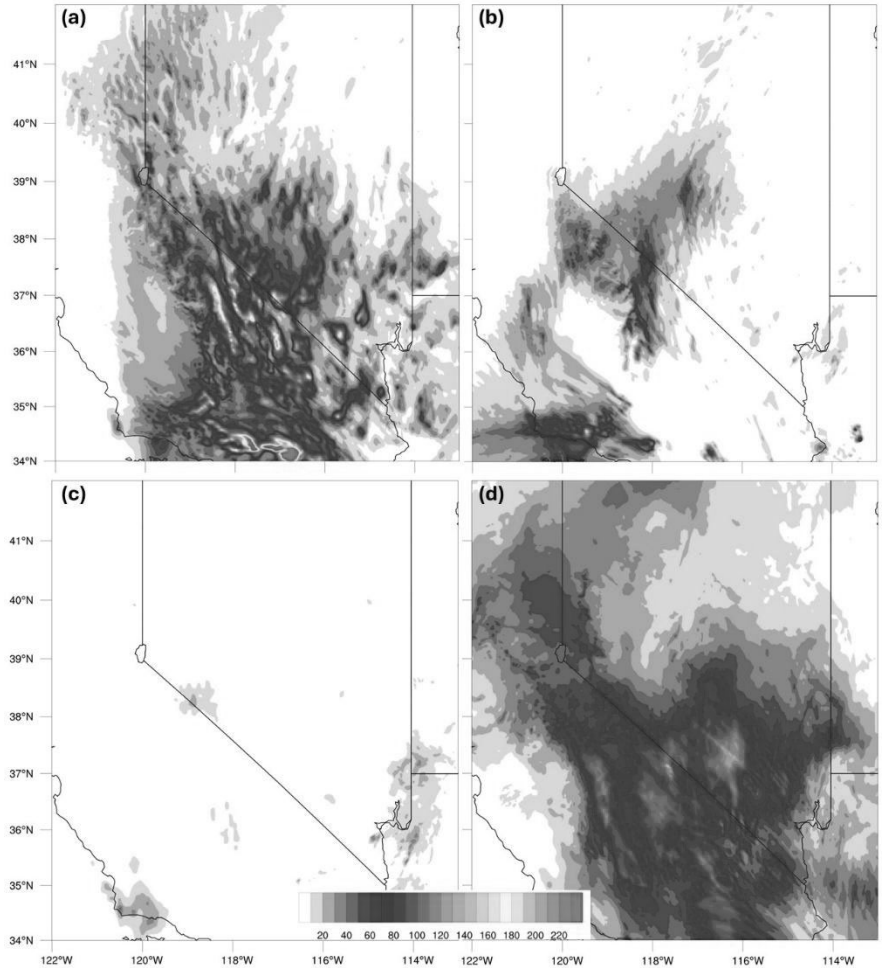

Figure 14. D02 WRF-ARW simulated accumulated rainfall (mm) valid from 2100 UTC 19 August to 2100 UTC 20 August 2023 for CTRL (**a**), NHMFL (**b**), NHMFLO (**c**), and ST (**d**).

Figure 15 shows the model terrain height m along with five cross-sections: Reno, NV (REV), to Elko, NV (LKN); Oakland, CA (OAK), to Salt Lake City, UT (SLC); Las Vegas,

NV (VEF), to Grand Junction, CO (GJT); Vandenburg, CA (VBG), to Flagstaff, AZ (FGZ); and San Diego, CA (NKX), to Tucson, AZ (TUS). Within central and southern NV, the terrain heights are heterogeneous due to localized mountain ranges. The most impactful cross-sections from the CTRL and NHMFL simulations are OAK to SLC and VBG to FGZ.

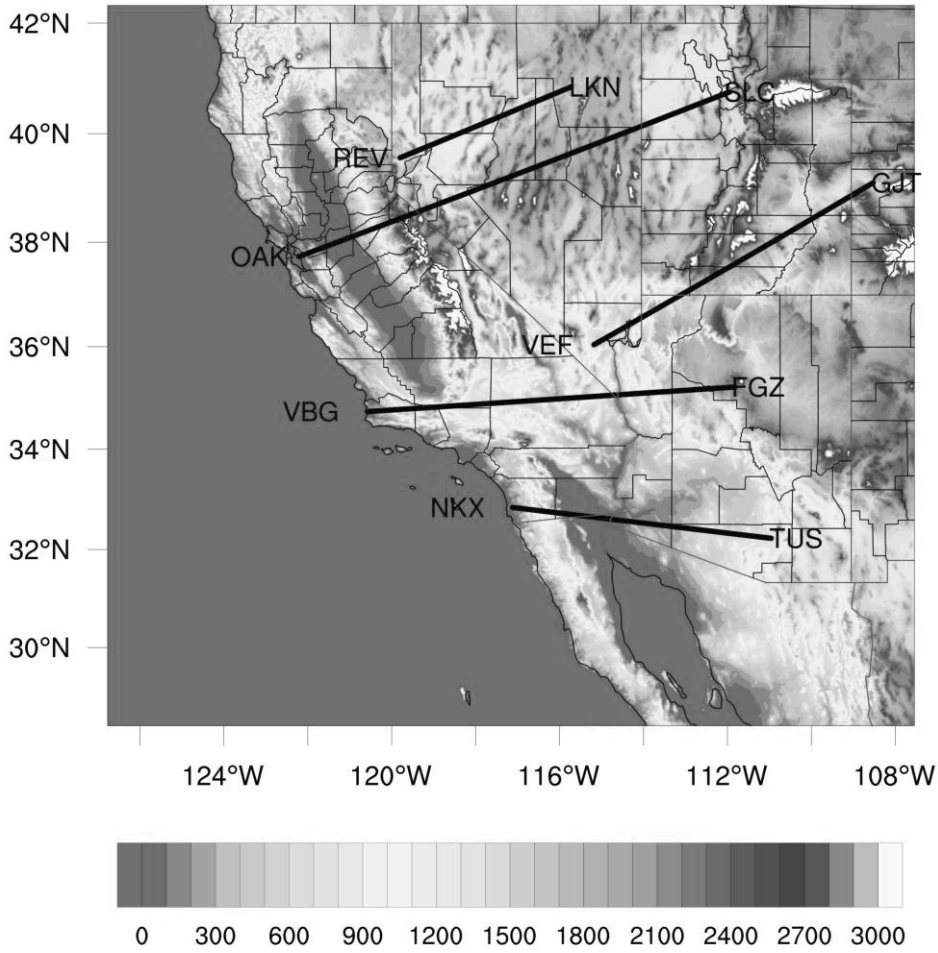

Figure 15. D02 WRF-ARW simulated terrain (elevation in m; color) and notable cross-sections: Oakland, CA (OAK), to Salt Lake City, UT (SLC), and Vandenburg, CA (VBG), to Flagstaff, AZ (FGZ).

Figure 16 shows the OAK to SLC cross-section of wind speed and vectors. Panels a-c represent the CTRL while d-f represent the NHMFL valid for 0000 UTC, 0600 UTC, and 1200 UTC 20 August for panels a-c and d-f, respectively. In Figure 16a, the CTRL simulation captures the various MPS circulations (40.1° N, −114.2° W) to (40.5° N, −112.8° W), (39.3° N, −116.9° W) to (39.7° N, −115.5° W), and centered at (38.9° N, −116.9° W). With these MPS circulations, the upward motion induced by surface heating exists prior to the formation of the mid-level jet. Six hours later, jetogenesis begins from 500–600 hPa and strengthens to wind velocities ~38 ms^{-1} in Figure 16c. The NHMFL simulation shows substantially different results. The various MPS circulations do not exist and a notable change in wind direction occurs below 450 hPa (Figure 16d). With time, mid-level jetogenesis occurs within an upward motion region of the large-scale MPS. However, this feature is inconsistent with the observational wind speed/direction analysis in Figure 16e.

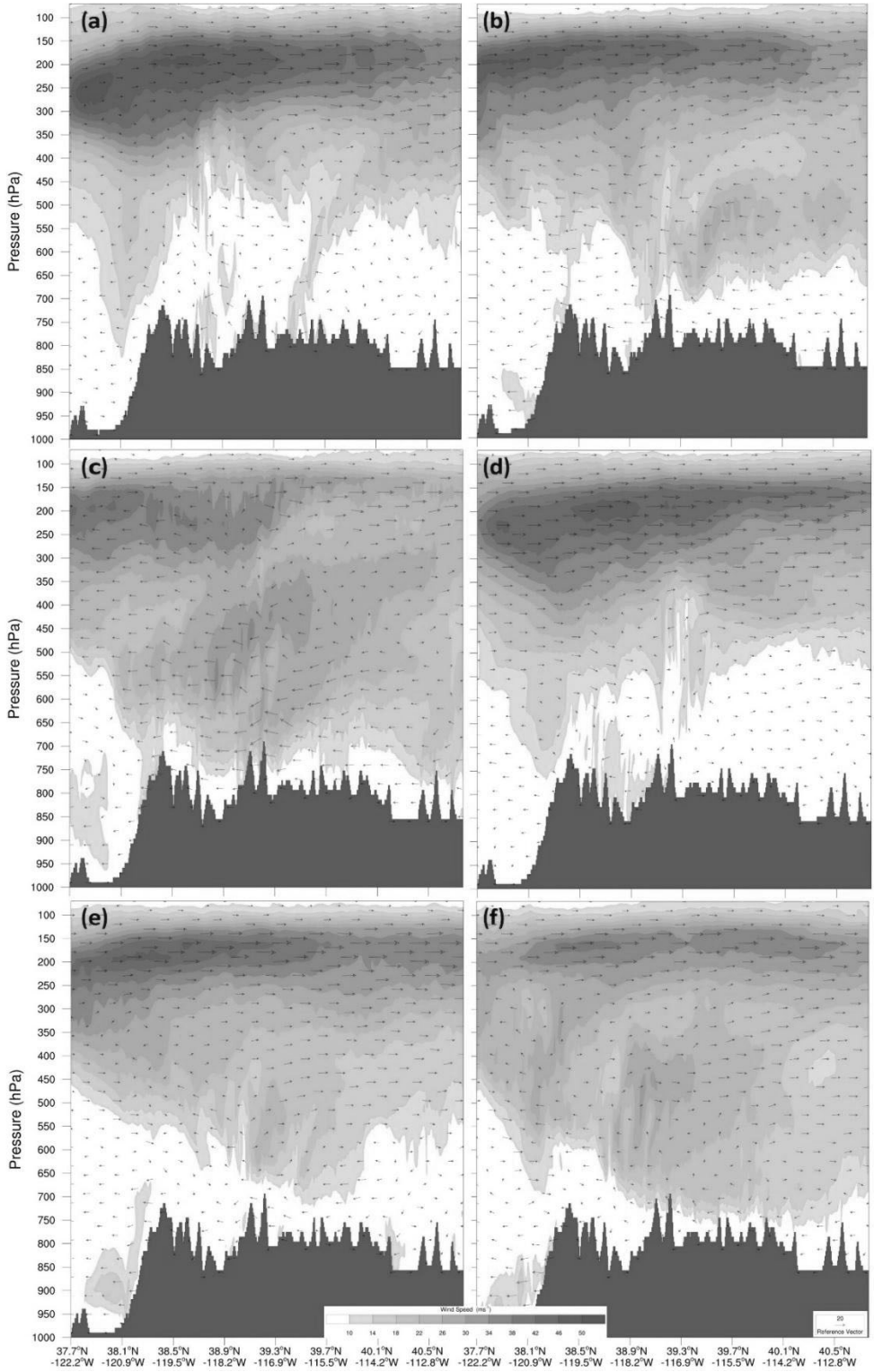

Figure 16. D02 WRF-ARW simulated cross-section from Oakland, CA (OAK), to Salt Lake City, UT (SLC), valid on 20 August for 0000 UTC (**a**,**d**), 0600 UTC (**b**,**e**), and 1200 UTC (**c**,**f**) for CTRL and NHMFL, respectively, with isotachs in color and wind vectors. Units are ms^{-1}.

Figure 17 shows the VBG to FGZ cross-section depicting the same times and variables as Figure 16. Since this cross-section is at a lower latitude than OAK to SLC, the mid-level jet transects this cross-section earlier in Figure 17a (CTRL). The mid-level jet rapidly increases in both size and magnitude in Figure 17b. By 1200 UTC 20 August (Figure 17c), the mid-level jet has intensified to 46 ms^{-1} and extended to the surface as it begins interacting with the TC remnant circulation's outer bands. In the NHMFL simulation,

jetogenesis fails to initiate in Figure 17d, with nearly unsheared flow below 600 hPa. By 0600 UTC 20 August, an extension of the upper-level jet begins descending but lacks magnitude and heterogeneity within the mid-levels. By 1200 UTC 20 August, the upper-level jet exits the region, leaving an ambiguous mid-level jet circulation, but compared to Figure 17c, the scale and magnitude of the mid-level jet are different. This supports the importance of the heat and moisture fluxes priming the environment for significant jetogenesis. Without heat and moisture fluxes, the simulated mid-level jet differs from the observed jet, forming by a different mechanism and not extending to the surface.

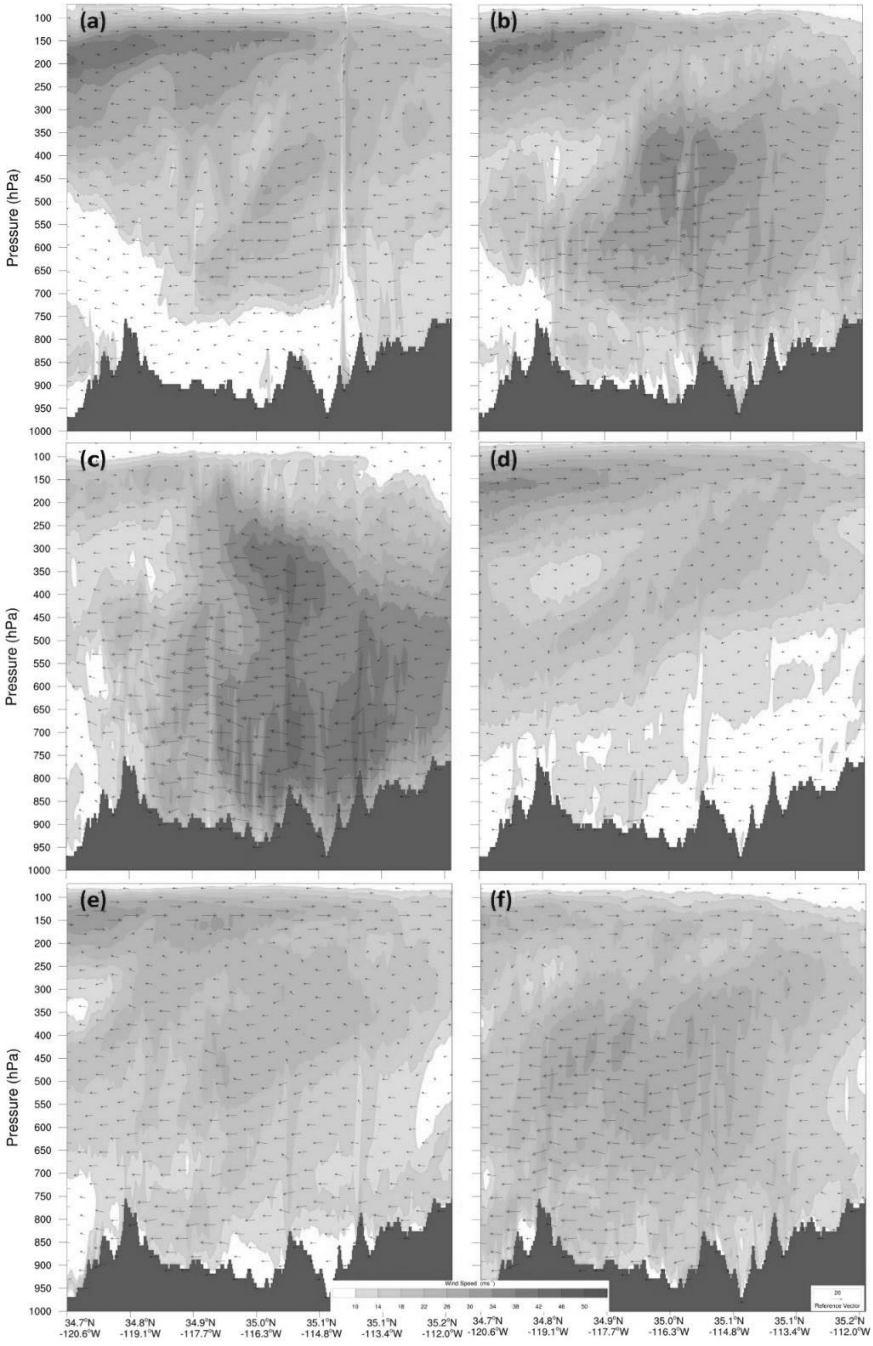

Figure 17. D02 WRF-ARW simulated cross-section from Vandenburg, CA (VBG), to Flagstaff, AZ (FGZ), valid on 20 August for 0000 UTC (**a**,**d**), 0600 UTC (**b**,**e**), and 1200 UTC (**c**,**f**) for CTRL and NHMFL, respectively, with isotachs in color and wind vectors. Units are ms^{-1}.

Figure 18 depicts the vertical profile of the 316 K isentrope over eastern NV into western UT and western AZ. This is valid at 0600 UTC 20 August for all cases: CTRL, NHMFL,

NHMFLO, and ST. Pressure (hPa) is shaded, and relative humidity is in contoured %. Figure 18a shows the pressure differences on the 316 K surface. Over central NV, the isentrope varies little with an average pressure of ~575 hPa. In line with the heated regions of the Great Basin, the isentrope descends substantially over eastern NV in less than 10 km, and the pressure changes from ~575 hPa to ~725 hPa, which induces mid-level jetogenesis through a significant horizontal pressure gradient on the sloping isentropic surface. RH also increases by 40% on that sloping isentrope, which is associated with simulated convective activity because of the increase in dewpoint temperatures. The NHMFL simulation in Figure 18b exhibits a much weaker pressure gradient along the isentrope while maintaining larger RH values over central NV. The pressure gradient of 25 hPa/10 km over central NV is significantly smaller than that of the CTRL and more importantly is oriented nearly perpendicular to the CTRL gradient. Further modification of the heat and moisture fluxes (Figure 18c), in NHMFLO, stabilizes the atmosphere more than the simulated atmosphere in Figure 18b. Without heat and moisture fluxes, the atmosphere is closer to static stability rather than simulated convective instability. Pressure varies little over NV, southern CA, western AZ, and UT, while the RH plume reverses its structure compared to the CTRL. Figure 18d depicts the ST simulation atmosphere which can be compared to the CTRL. Higher-magnitude RH is simulated over central NV while a substantial yet more localized pressure gradient of ~575 hPa to ~750 hPa in 100 km has formed over western UT. Inferences can be made regarding the effects of complex terrain on the interactions of the mid-level jet.

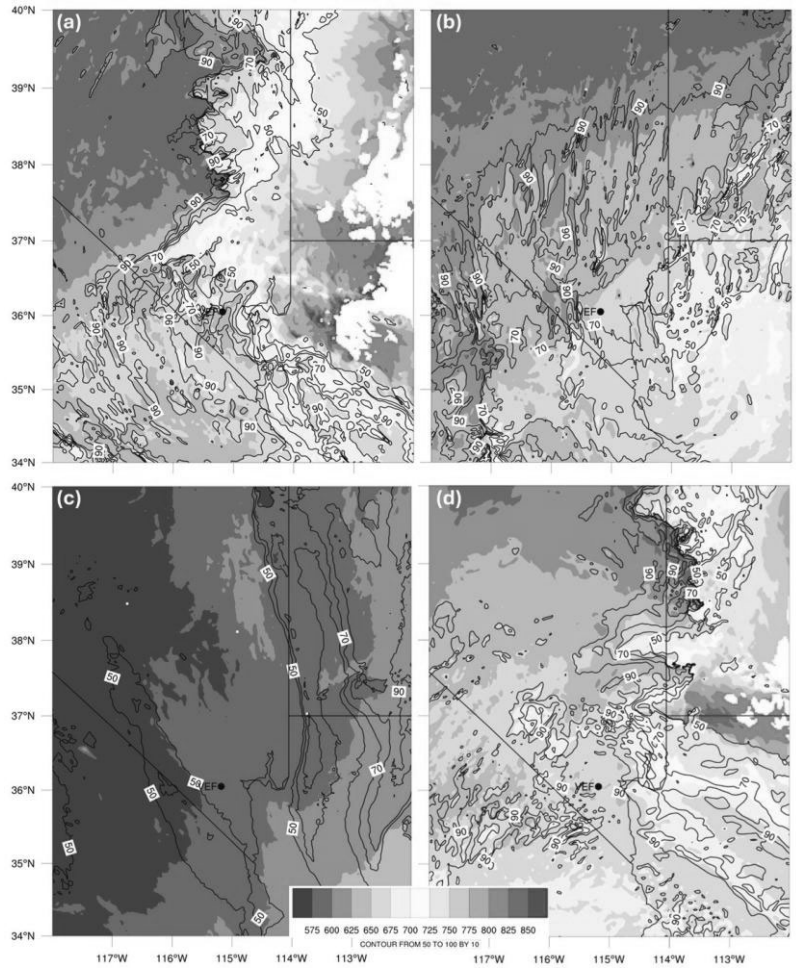

Figure 18. D02 WRF-ARW simulated isentropic analysis on the 316 K surface showing pressure in color (hPa) and relative humidity (RH, %) in contours, valid at 0600 UTC 20 August for CTRL (**a**), NHMFL (**b**), NHMFLO (**c**), and ST (**d**).

https://doi.org/10.3390/atmos17010082

Figure 19 shows wind velocity (shading in ms^{-1}) and the Montgomery Stream Function (contours of ψ in m^2s^{-2}) for all simulated 316 K isentropes valid at 0600 UTC 20 August. Figure 20a depicts the consequences of the significant pressure gradient, as in Figure 18. The mid-level jet forms parallel to the maximum pressure gradient and can be distinguished from the TC remnant circulation as the jet contains wind velocity values of 32 ms^{-1}. Figure 19b shows less variation in faster wind velocities with larger ψ values. Parallel to the perpendicular pressure gradient, seen in Figure 18b, stronger wind velocities form and exhibit a bimodal circulation over western-central NV. However, the wind velocity decreases by 10 ms^{-1} and is oriented diagonally to the observed jet. Consistent with the lack of heat and moisture fluxes over land, the TC remnant circulation falls apart faster after landfall. In Figure 19c (NHMFLO), no mid-level jet feature exists, with even larger yet less varying values of ψ. In Figure 19d, the smoothed terrain renders a faster-propagating TC remnant circulation with higher wind velocity values, ~36 ms^{-1}, but a less distinguishable mid-level jet. This is likely induced by considerably weaker orographic effects. Therefore, the complex terrain, surface heat fluxes, and moisture fluxes play significant roles in the formation, maintenance, and propagation of the mid-level jet.

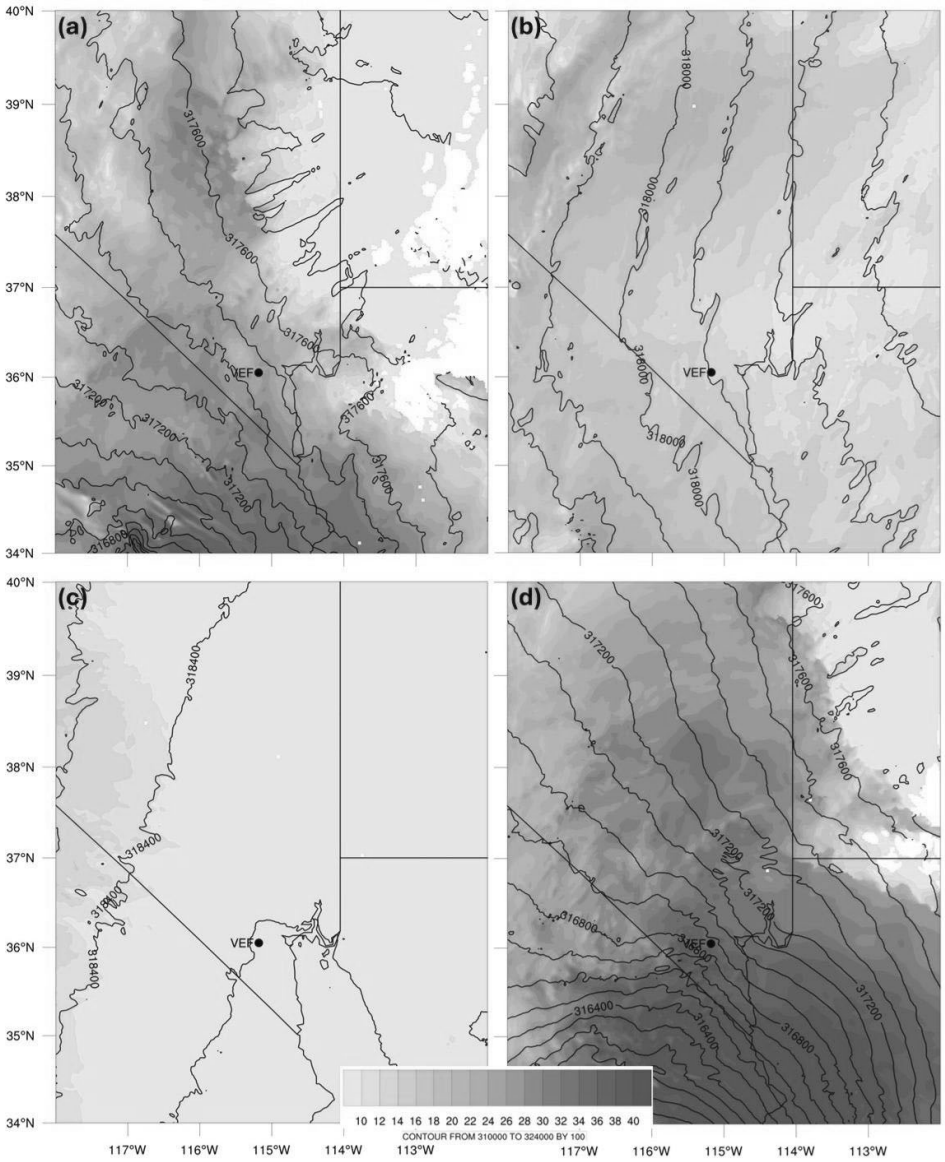

Figure 19. D02 WRF-ARW simulated isentropic analysis on the 316 K surface showing isotachs in color (ms^{-1}) and the Montgomery Stream Function (ψ, m^2s^{-2} in contours, valid at 0600 UTC 20 August for CTRL (**a**), NHMFL (**b**), NHMFLO (**c**), and ST (**d**).

https://doi.org/10.3390/atmos17010082

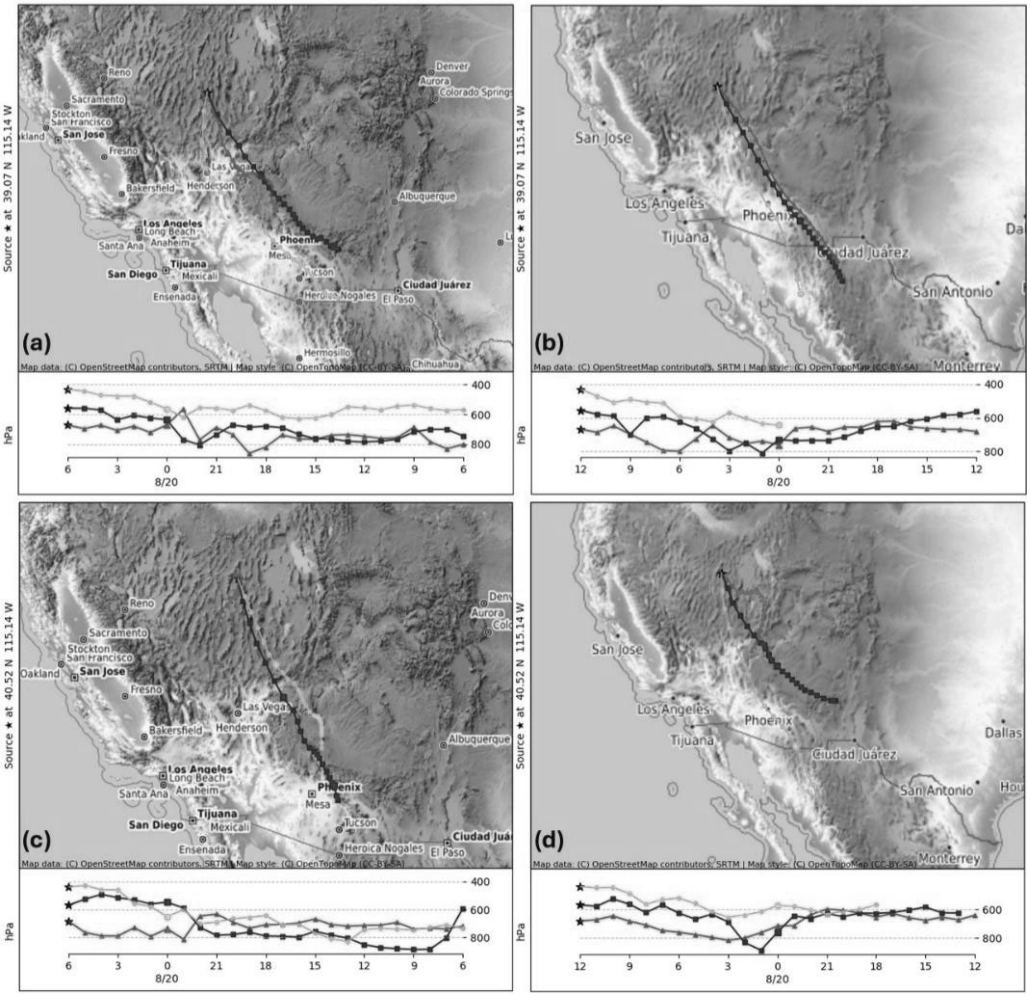

Figure 20. WRF ARW D02 backward trajectories derived using NOAA's HYSPLIT model [22]. Red contour = 1.5 km-AGL; blue contour = 3 km-AGL; green contour = 5 km-AGL. Panels (**a**,**c**) and (**b**,**d**) are valid for 0600 UTC and 1200 UTC 20 August, respectively. Panels (**a**,**b**) show backward trajectories for 322 km North of Las Vegas, NV (black star), while (**c**,**d**) show backward trajectories at 483 km north of Las Vegas, NV (black star).

Figure 20 depicts the NOAA Hybrid Single-Particle Lagrangian Integrated Trajectory (HYSPLIT) model [22] analysis of the WRF-ARW D02 simulation parcel transport. Figure 20a,b show backward parcel trajectories for the location corresponding to ~322 km poleward of Las Vegas, NV, for 0600 UTC and 1200 UTC 20 August, respectively. Figure 20c,d represent the location corresponding to ~483 km poleward of Las Vegas, NV. In addition, the backward trajectories are constrained to fit the previous 24 h. The air parcels were released at altitudes of 1.5 km-AGL (red), 3 km-AGL (blue), and 5 km-AGL (green) which roughly represent 700–425 hPa for Figure 20. For geographical locations, refer to Appendix A, Figure A2. Figure 20a indicates that the air parcels released in the 600–700 hPa layer originate from central AZ, while the 425 hPa air parcel originates from southern AZ. Tracing back the red and blue contours from the final position above Las Vegas, NV, shows the air parcels accelerating northwestward from western AZ to central NV. Prior to 2200 UTC 19 August, the air parcels were oscillating in proximity to the 750 hPa layer. However, near the time of jetogenesis, the air parcels are lifted to the 650–600 hPa level and gain momentum as shown by the increased distance between data points nearing the star location. Similarly for the 5 km-AGL air parcel, as it approaches Las Vegas, NV, from the south, it accelerates and is lifted from ~600 hPa to ~425 hPa. Therefore, an interaction exists along the boundary of the cloud shield of the incoming TC circulation in conjunction with

the elevated surface heating lifting the air parcels. Also, in Figure 20b, the air parcels take a similar path but extend further equatorward into Mexico. By 1200 UTC 20 August, the mid-level jet had expanded with a wind velocity > 30 ms^{-1}. With the increased air parcel velocity, as traced back to 0000 UTC 20 August, the corresponding air parcels accelerate and rise rapidly with a displacement of nearly 200 hPa within 12 h towards the north-northwest. Figure 20c indicates a slower and less varying air parcel near the 700 hPa level, as it moves from near 160 km poleward of Las Vegas, NV, to ~483 km poleward of Las Vegas, NV, within the previous 24 h. The 3 km-AGL and 5 km-AGL air parcels again originate near central AZ, with slower velocities until 2200 UTC 19 August. Although their direction remains unchanged, once air parcels cross the boundary of the maximum pressure gradient—marking the shift from stable desert to tropical airmass—they accelerate rapidly and rise ~200 hPa within eight hours. For Figure 20d, the parcel released around the jetogenesis level, i.e., ~600 hPa, exhibits a clockwise turning in time, starting at 1300 UTC 19 August. Although the level at which the air parcel can be traced back in time and space does not vary prior to 0100 UTC 20 August, considerable ageostrophic forcing takes place in the change in direction of the air parcel as it traverses northwestward and accelerates at 0100 UTC 20 August, this time with a vertical displacement of ~275 hPa.

4.3. Ageostrophic Diagnostics

Consistent with Wolf and Johnson [2], the ageostrophic motion of air parcels can be diagnosed to determine the relative impact of isallobaric, inertial advective, and inertial diabatic forcing functions on the formation and maintenance mechanisms of the mid-level jet. The isallobaric motion represents the portion of the ageostrophic wind arising from the time tendency of the horizontal pressure gradients in the isentropic coordinate system. For inertial advective motion, non-uniform spatial differences in geostrophic wind, i.e., differences in the actual wind from the geostrophic wind due to advection, dominate. For inertial diabatic ageostrophic motion, heating or cooling of the surface results in the forcing of air parcels to cross isentropic surfaces, resulting in an upward (downward) mass flux depending on the rising (sinking) motion of the air parcel relative to the isentropic level. A brief analysis of the individual ageostrophic wind forcing terms will be given for the CTRL, and the total ageostrophic motion for the CTRL and NHMFL simulations will be diagnosed. The following analysis will be given from D01, made simpler due to a smoother set of dependent variables.

Figure 21 represents the isallobaric component (ms^{-1}) valid for 0600 UTC, 1200 UTC, and 1800 UTC 20 August depicted on the 308 K (low-level) (Figure 21a–c) and 320 K (mid-level) isentropes (Figure 21d–f) for the CTRL. At 0600 UTC 20 August, the isallobaric ageostrophic component is extremely weak across the 308 K isentrope. However, because of the vertical variation in the horizontal pressure gradient existing from west to east in Figure 18, with time (Figure 21b), the isallobaric component increases and is directed towards the steepest slope of the isentrope. In Figure 21c, the isallobaric component shifts equatorward and isallobaric forcing accelerates air motion from 35.5° N to 35.95° N. This equatorward repositioning of isallobaric forcing is indicative of a strengthening east–west pressure gradient. However, on the 320 K isentrope (Figure 21d), a moderate northeastward-directed isallobaric flow is found with accelerations diagonally across the domain. In Figure 21e, the flow changes to be primarily eastward with near-constant velocity. By 1800 UTC 20 August, the mid-level isallobaric forcing of the air motion rotates primarily equatorward to south-southeast from northern NV to southeast CA. This mid-level flow shows weak acceleration and clockwise rotation over 12 h, indicating a strengthening high-pressure area on the 320 K surface due to mass convergence in the lower troposphere.

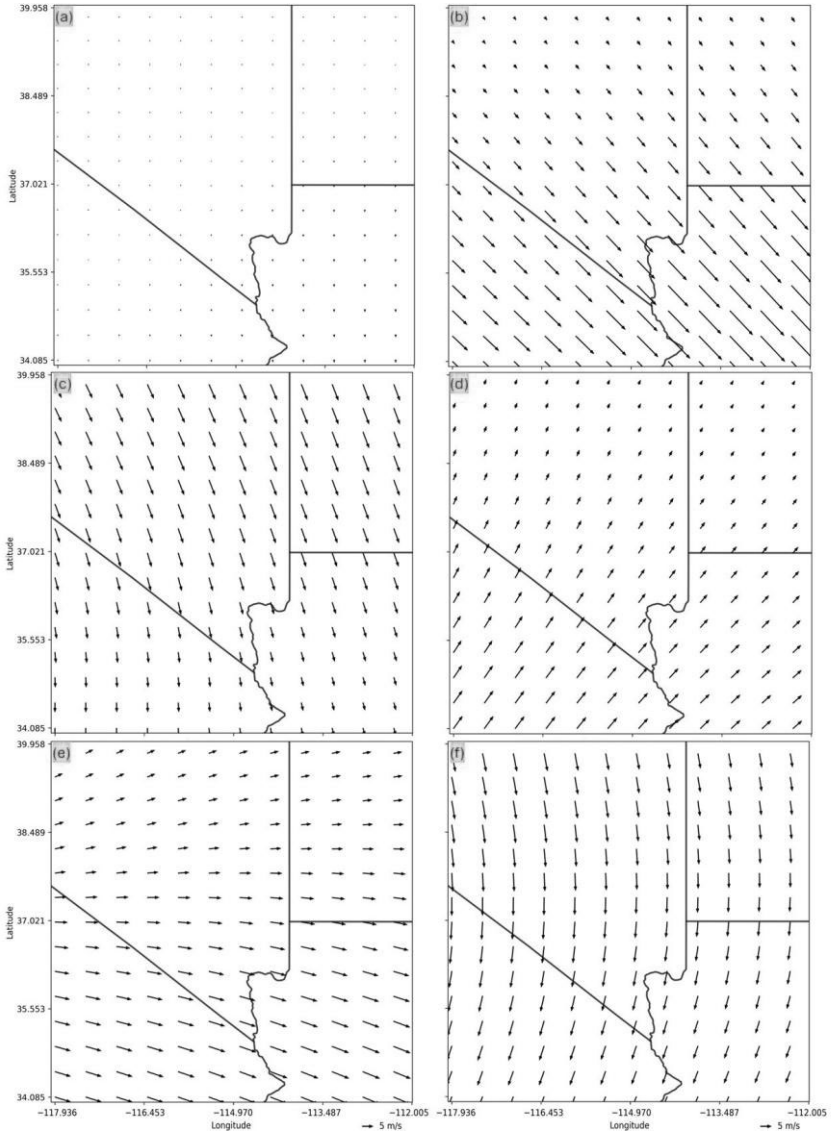

Figure 21. D01 WRF-ARW simulated isallobaric ageostrophic motion in vectors (ms^{-1}) on the 308 K isentropic surface (**a**–**c**), and the isentropic 320 K surface (**d**–**f**) valid for 0600 UTC, 1200 UTC, and 1800 UTC August 2023, respectively, for CTRL.

For inertial advective motion, Figure 22 displays the same time intervals and isentropes in ms^{-1} as those in Figure 21. A weak inertial advective signal is shown in the northern portion of NV and western UT, but the inertial advective signal accelerates equatorward and begins to generate a line of convergence in western AZ. By 1200 UTC 20 August (Figure 22b), the convergence zone has moved poleward, spanning much of southern CA, southern NV, and part of northwestern AZ, and extending into southwestern UT. A strong inertial advective signal exists, ranging from 20–30 ms^{-1}, which is displaced between convergence zones. Furthermore, a westward-directed inertial advective signal is also established in western UT. As convergence increases, air parcels ascend and accelerate, leading to a strengthening mid-level jet over time. By 1800 UTC 20 August (Figure 22c), the stronger northwestward-directed inertial advective motion has propagated six degrees poleward, consistent with the propagation speed of the mid-level jet. On the 320 K isentrope, a similar sequence of inertial advective forcing to 308 K exists. However, the magnitude of the inertial advective term decreases on this isentrope because the influence of low-level forcing weakens vertically. This indicates that the mid-level jet developed from low-level forcing rather than direct upper-level jet forcing.

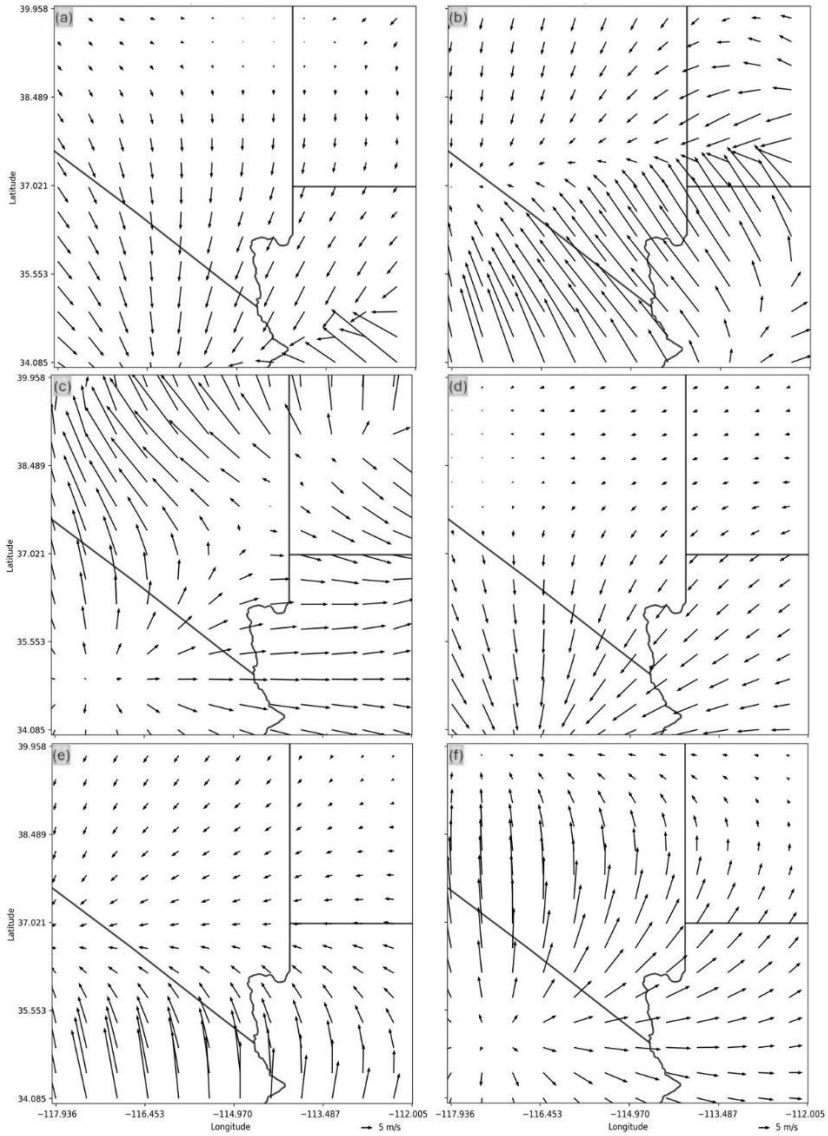

Figure 22. D01 WRF-ARW simulated inertial advective ageostrophic motion in vectors (ms^{-1}) on the 308 K isentropic surface (**a**–**c**), and the isentropic 320 K surface (**d**–**f**) valid for 0600 UTC, 1200 UTC and 1800 UTC 20 August 2023, respectively, for CTRL.

The final term is inertial diabatic forcing. Figure 23 shows the same time periods and isentropes as the other terms. Figure 23a initially shows negligible diabatic forcing on the 308 K isentrope poleward of 35.5° N, but equatorward inertial diabatic forcing begins to increase from east to west. Later in Figure 23b, the inertial diabatic forcing propagated poleward into southern NV and encompasses most of southern CA and western AZ. The persistent east-to-west-directed inertial diabatic forcing highlights the significant role of elevated surface heating in the clear, warm, and dry desert regions to the east-northeast, in contrast to the relatively cloudy, cool, and humid regions influenced by the marine boundary layer to the west-southwest near the TC. In Figure 23c, the inertial diabatic forcing has progressed and maximized near eastern NV and is directed into the mid-level jet. However, on the 320 K isentrope, the increased elevation reduces impacts from this term, as seen from negligible forcing through this 12 h period in Figure 23d–f.

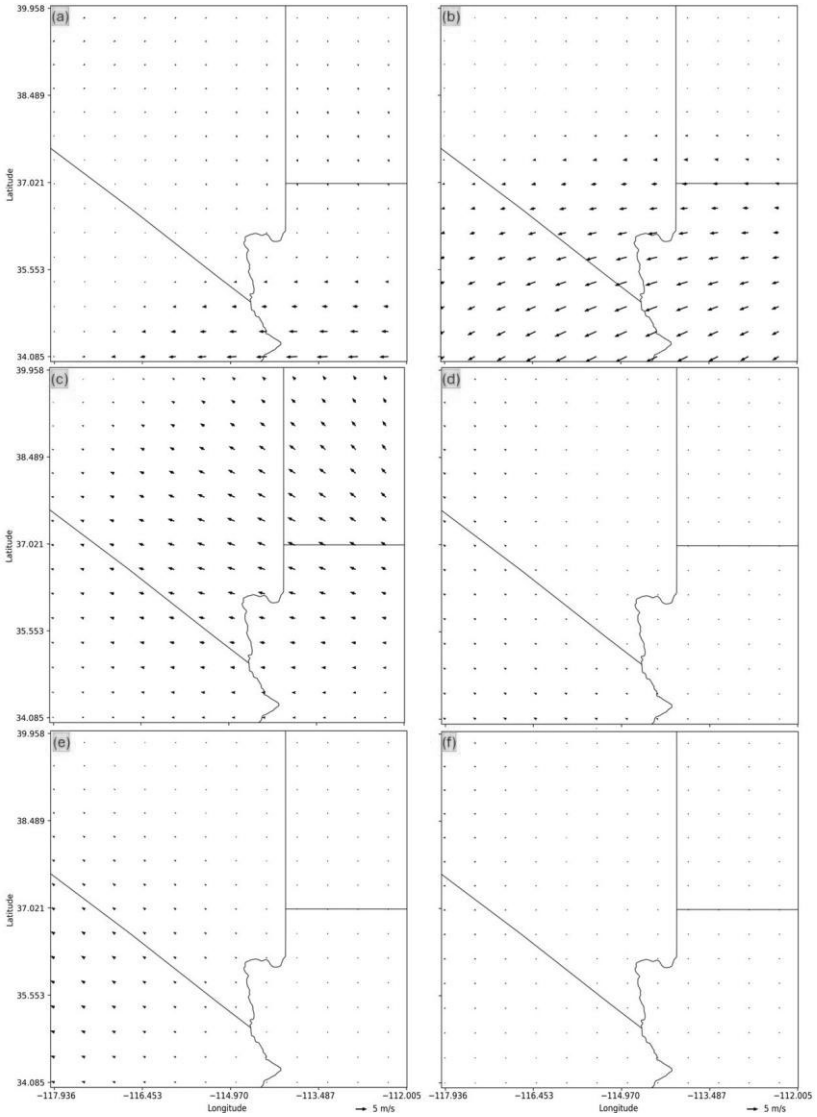

Figure 23. D01 WRF-ARW simulated inertial diabatic ageostrophic motion in vectors (ms^{-1}) on the 308 K isentropic surface (**a**–**c**), and the isentropic 320 K surface (**d**–**f**) valid for 0600 UTC, 1200 UTC, and 1800 UTC 20 August 2023, respectively, for CTRL.

Figure 24 shows the total ageostrophic motion by combining the three terms. The inertial advective and isallobaric terms have the greatest influence on mid-level jetogenesis and would attribute the most to parcel acceleration propagating poleward. Figure 24a shows the ageostrophic motion on the 308 K isentrope with the significant change in ageostrophic motion in eastern AZ from southwest–northwest. In Figure 24b, the convergence propagated poleward with the east-to-west-directed flow from western UT into the entrance region of the mid-level jet in eastern NV. In north-central NV, the ageostrophic motion intensifies and propagates equatorward. Later in Figure 24c, the strongest ageostrophic motion has exited the plot poleward into northern NV along with stronger accelerations. On the 320 K isentrope, the overall ageostrophic motion is weaker than that of the 308 K isentrope, but the rotation of the wind vectors is impactful. Ageostrophic motion is initially weaker poleward of 37° N in Figure 24d, but a convergence zone remains present in southern CA, though less pronounced than in Figure 24a. Six hours later in Figure 24e, a stronger poleward propagation of ageostrophic wind exists equatorward of 36° N; however, by 1800 UTC 20 August, areas of convergence shown in Figure 24c are replaced by divergence in Figure 24f, which indicates the importance of converging and rising ageostrophic motion below the mid-level jet and diverging motion above the mid-level jet.

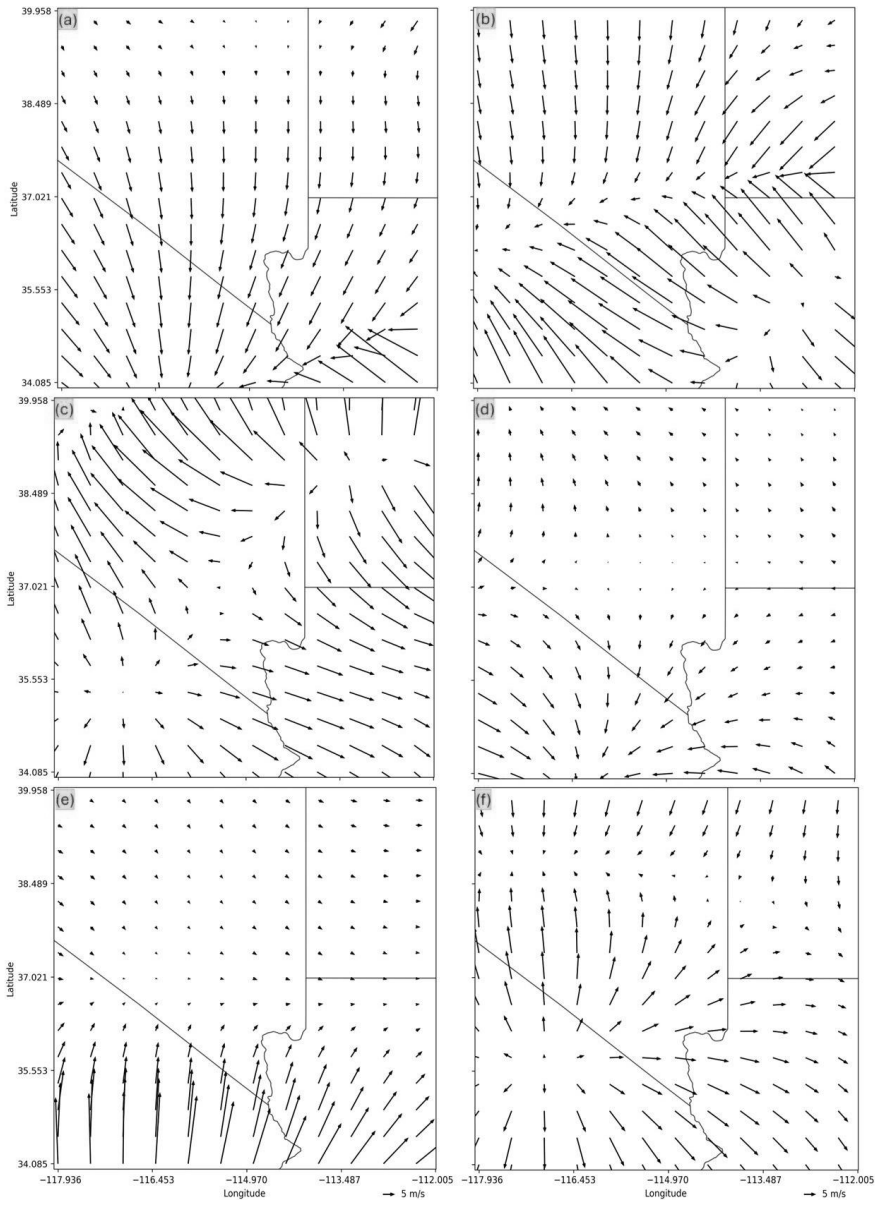

Figure 24. D01 WRF-ARW simulated total ageostrophic motion in vectors (ms^{-1}) by summation of the isallobaric, inertial advective and inertial diabatic ageostrophic terms on the 308 K isentropic surface (**a**–**c**), and the 320 K isentropic surface (**d**–**f**), valid for 0600 UTC, 1200 UTC, and 1800 UTC 20 August 2023, respectively, for CTRL.

In the NHMFL simulation, total ageostrophic motion is considerably weaker due to the lack of surface-based heat and moisture fluxes. On the 308 K isentrope (Figure 25a), near-zero motion exists, except around central UT and southwestern AZ, while Figure 25b shows weak and diverging motion over southern NV which should be the mid-level jet. Figure 25c shows minimal yet equatorward flow over what should have been the mid-level jet. However, the dynamics of the lower troposphere appear to be more stable and less turbulent. On the 320 K isentrope, relatively uniform ageostrophic motion is simulated with minimal flow changes with time, in Figure 25d–f, with no significant convergence or divergence. Therefore, without heat and moisture fluxes over land, the favorable lower tropospheric dynamics are negligible and decoupled from any ageostrophic motion to accelerate air parcels.

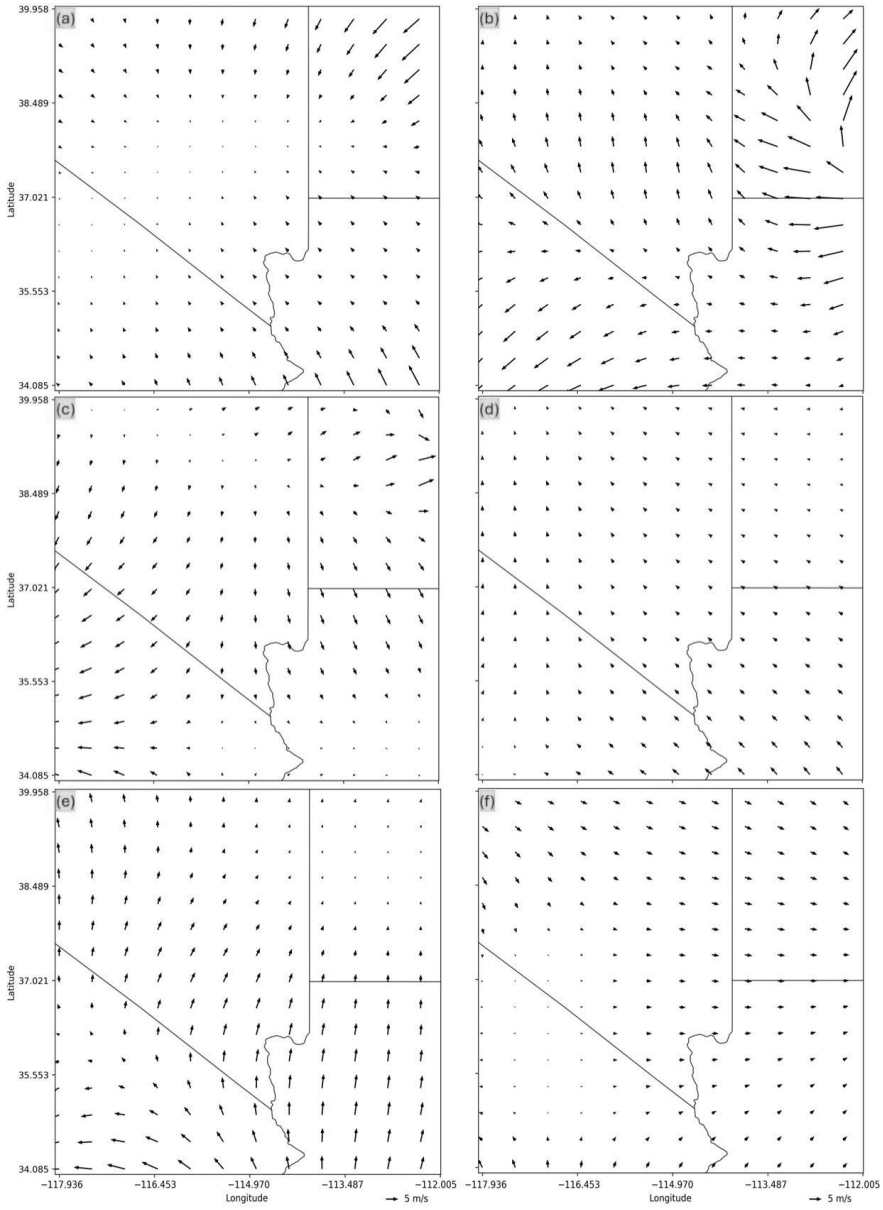

Figure 25. D01 WRF-ARW simulated full motion in vectors (ms^{-1}) by summation of the isallobaric, inertial advective and inertial diabatic ageostrophic terms on the 308 K isentropic surface (**a**–**c**), and the 320 K isentropic surface (**d**–**f**), valid for 0600 UTC, 1200 UTC, and 1800 UTC 20 August 2023, respectively, for NHMFL.

5. Conclusions

This manuscript examined the downstream jetogenesis and its implications for inland precipitation prior to landfall of TC Hilary (2023). This mid-level jet altered the downstream environment by transporting moisture more than 1000 km into the Great Basin and modifying the ascent responsible for MCS formation.

The mid-level jetogenesis over eastern NV resulted from atmospheric dynamical processes involving low-level heating from the arid region of the southwestern U.S. juxtaposed with the relatively cooler marine boundary layer in southern CA and the Sierra Nevada. The available observations of the MCSs that formed from mid-level jetogenesis were adequately represented in the CTRL simulation in time, geographical location, intensity and scale. Three additional sensitivity experiments were performed to explain the mechanisms for mid-level jetogenesis: NHMFL, NHMFLO, and ST. The NHMFL and NHMFLO simulations removed the heat and moisture fluxes over land and both land and

ocean, respectively, for the duration of the simulations while the ST simulation performed additional smoothing passes over the complex terrain.

As depicted in the NHMFL simulation, the moderate temperature gradient over eastern NV was eliminated because of the more uniform temperature profile over the Great Basin. However, the marine PBL did not change drastically, as evidenced in the Qv analysis. In the NHMFLO simulation, the temperature profiles over the southwestern U.S. become more uniform and the marine PBL becomes more stable due to the lack of moisture transport from ocean to land. In the ST simulation, the notable temperature gradient still exists in configuration and magnitude as well as moderate Qv located in southern NV. In the NHMFL and NHMFLO simulations, the mid-level jet is eliminated and there is considerably less precipitation in southern CA and NV.

Over the southwestern U.S., the NHMFL and NHMFLO simulations depict less static instability compared to the CTRL simulation's convective instability. With the lack of heat and moisture fluxes, the continental PBL remains shallow and stable. This prevents air parcels from crossing isentropic surfaces, generating the lift necessary for jetogenesis and subsequent MCSs to form as seen from the lack of > 200 hPa pressure gradient in the NHMFL and NHMFLO simulations. Evidence of this lift in air parcels is in the backward trajectory analysis of the CTRL. In the ST simulation, the significant pressure gradient still exists over the complex topography but has shifted eastward due to the smoothing of the localized complex topography in eastern NV and western UT. The reduction in surface friction adversely affects mid-level jet formation, as the increased ground velocity of Hilary's remnant circulation over land does not allow sufficient time for the development of the mid-level jet.

In summary, the sensitivity simulations and ageostrophic diagnostics indicate that the mid-level jet was the product of the differential surface heating between the Great Basin and CA coast. In the ageostrophic diagnostic analysis, the isallobaric forcing proves to be significant in the development of the mid-level jet, but the inertial advective term is dominant by forcing convergence near its entrance region.

This manuscript shows the importance of the dynamical processes associated with the remnant passage of TC Hilary in the southwestern U.S. Due to the rarity of landfalling TCs along the western seaboard of the U.S., further case studies are needed to explore the different atmospheric dynamical processes of similar TC landfalls compared to TC landfalls around the Gulf of Mexico and the U.S. eastern seaboard. Finally, higher-resolution simulations would prove to be helpful in diagnosing the meso-γ interactions of barrier jets or blocking phenomena associated with microscale precipitation in the Great Basin region.

Author Contributions: Conceptualization, J.T.W. and M.L.K.; Methodology, J.T.W. and M.L.K.; Software, J.T.W.; Validation, J.T.W. and M.L.K.; Formal analysis, J.T.W.; Investigation, J.T.W.; Data curation, J.T.W.; Writing—original draft, J.T.W.; Writing—review and editing, J.T.W., M.L.K. and Y.-L.L.; Visualization, J.T.W.; Supervision, M.L.K.; Project administration, Y.-L.L.; Funding acquisition, Y.-L.L. All authors have read and agreed to the published version of the manuscript.

Funding: This research was funded by the National Science Foundation Grant 2022961, and NCAR/CISL for support of computing time under Project UNCT0005.

Data Availability Statement: The numerical model results for this study are too large to archive. Instead, all information to replicate the results is provided. The NCAR/CISL environment used, namelists, and postprocessing scripts are available at the following GitHub page. https://github.com/jacksonwiles/Mid-Level_Jetogenesis/ (accessed on 30 September 2025).

Conflicts of Interest: The authors have no known financial or personal conflicts of interest which could influence the work in this manuscript.

Appendix A

In Figure A1, time series analyses of observed precipitation (in brown) are given for six ASOS/METAR airport-based observation (OBS) stations: KBYS (Bicycle Lake Fort Irwin Army Air Field, CA), KDAG (Barstow Dagget Airport, CA), KDRA (Desert Rock Airport, NV), KEED (Needles Airport, CA), KLAS (McCarran International Airport, NV), and KLSV (Las Vegas Nellis AFB, NV). Additionally, the Rapid Refresh model analysis (RAP, F00) is given (in blue) to give a comparison of the available observations to those of a highly sophisticated operational mesoscale model. Lastly, all WRF-ARW D02 simulations are included to validate/compare the simulated precipitation to the actual precipitation for this study: CTRL, NHMFL, NHMFLO, and ST. The times of interest are from 19 August 00 UTC to 22 August 00 UTC 2023. For all stations, the RAP analysis shows positively correlated precipitation totals that, in most cases, far exceed the observations, except for KEED, therefore showing the difficulty in consistently resolving the low-level dynamics to accurately represent accumulated precipitation. For WRF-ARW simulations, respectable results are given for accumulated precipitation, even with ERA5-based initial and boundary conditions on a scale of 2× coarser resolution than that of RAP. Specifically, for KDRA, KLAS, and KLSV, the trend and magnitude of accumulated precipitation of the CTRL simulation closely match the OBS. For the WRF-ARW NHMFL and NHMFLO simulations, drastically lower amounts of precipitation accumulated, as expected, due to the lack of surface-based heat and moisture fluxes. This results in trace amounts of accumulation at all stations, except for the NHMFLO simulation at KEED. Finally, the WRF-ARW ST simulation amplifies the amount of accumulated precipitation at most stations and comes closer to matching the trend and magnitude of the RAP analysis, except for KBYS and KEED, due to the lack of orographic blocking upstream of the station locations. Therefore, the WRF-ARW simulations employed in this case study render respectable accumulated precipitation totals that are comparable to the RAP model and available observations. For ASOS/METAR weather station locations as well as other notable locations used throughout this manuscript, please refer to Figure A2.

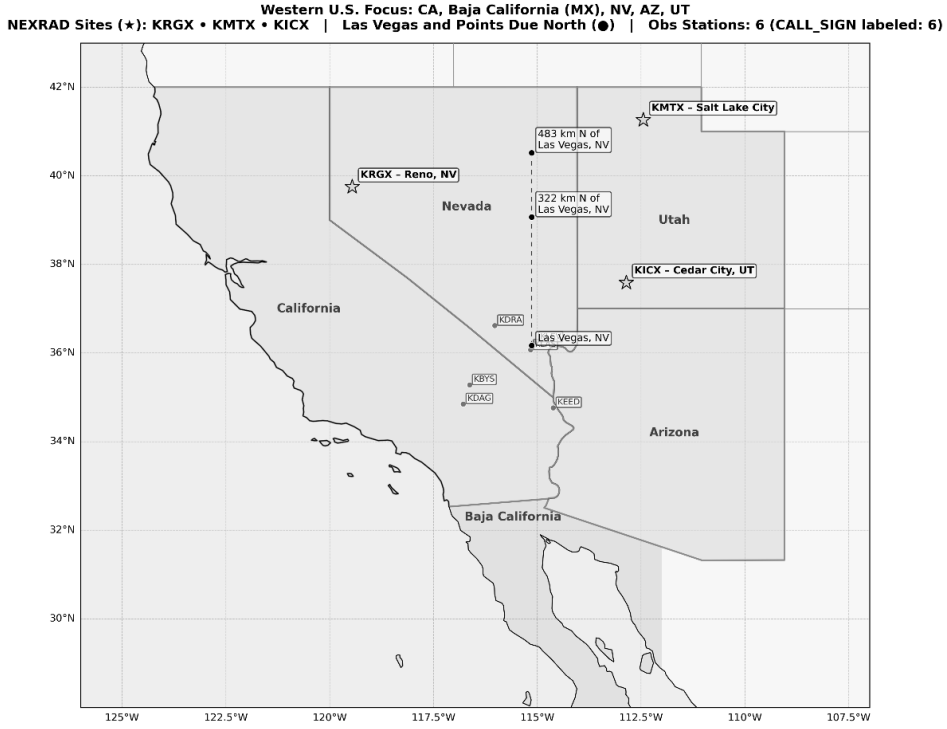

Figure A1. Notable geographical locations, NEXRAD sites (yellow stars), HYSPLIT air parcel locations (black filled circles), and ASOS/METAR weather stations (blue filled circles) used in this study.

https://doi.org/10.3390/atmos17010082

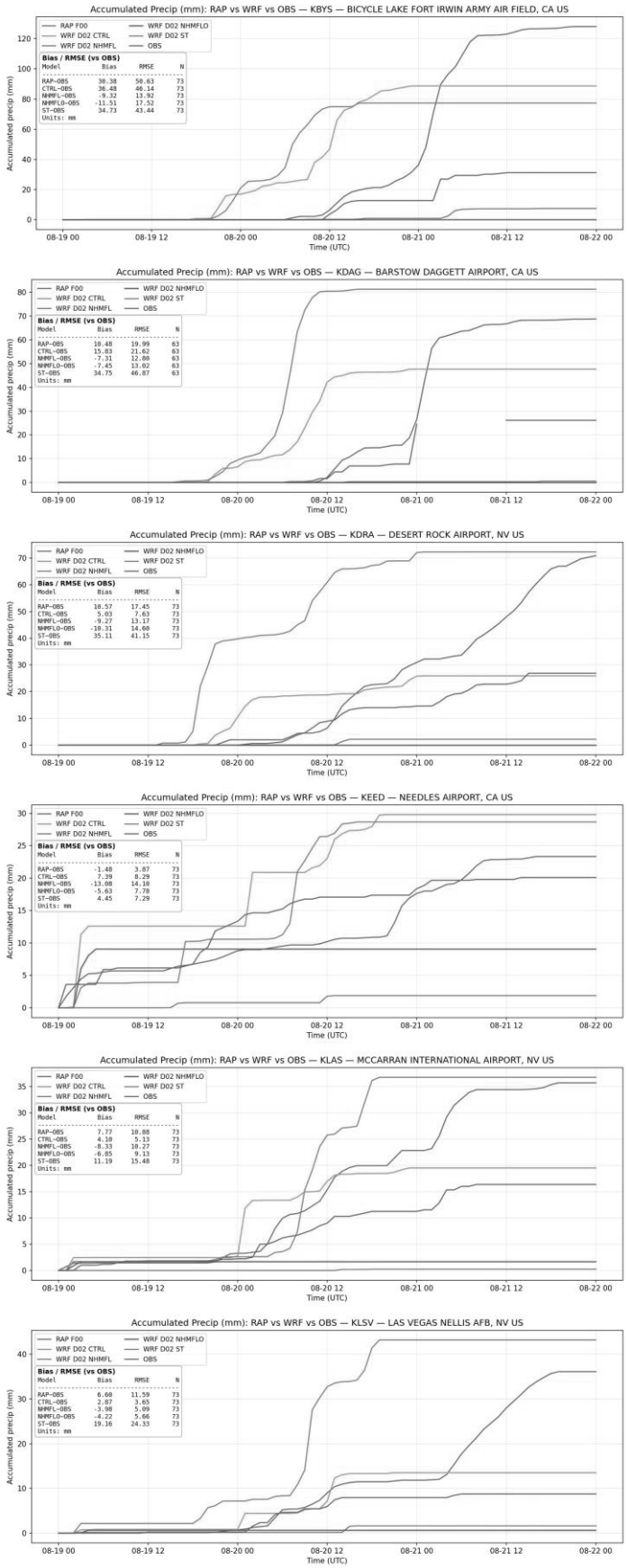

Figure A2. Time series analyses of accumulated precipitation from 0000 UTC 19 August to 0000 UTC 22 August, 2023, for the following ASOS/METAR weather stations: KBYS, KDAG, KDRA, KEED, KLAS, and KLSV. The legend is as follows: RAP (blue), WRF D02 CTRL (orange), WRF D02 NHMFL (green), WRF NHMFLO (red), WRF D02 ST (purple), and observations (OBS; brown).

References

1. Reinhart, B.J. National Hurricane Center Tropical Cyclone Report. Hurricane Hilary. 2024. https://www.nhc.noaa.gov/data/tcr/EP092023_Hilary.pdf (accessed on 14 February 2024).
2. Wolf, B.J.; Johnson, D.R. The Mesoscale Forcing of a Midlatitude Upper-Tropospheric Jet Streak by a Simulated Convective System. Part I: Mass Circulation and Ageostrophic Processes. *Mon. Weather Rev.* **1995**, *123*, 1059–1087. https://doi.org/10.1175/1520-0493(1995)123<1059:TMFOAM>2.0.CO;2.
3. Bao, X.; Zhang, F. Impacts of the Mountain–Plains Solenoid and Cold Pool Dynamics on the Diurnal Variation of Warm-Season Precipitation over Northern China. *Atmos. Chem. Phys.* **2013**, *13*, 6965–6982. https://doi.org/10.5194/acp-13-6965-2013.
4. Sun, J.; Zhang, F. Impacts of Mountain–Plains Solenoid on Diurnal Variations of Rainfalls along the Mei-Yu Front over the East China Plains. *Mon. Weather Rev.* **2012**, *140*, 379–397. https://doi.org/10.1175/MWR-D-11-00041.1.
5. Hua, S.; Xu, X.; Chen, B. Influence of Multiscale Orography on the Initiation and Maintenance of a Precipitating Convective System in North China: A Case Study. *J. Geophys. Res. Atmos.* **2020**, *125*, e2019JD031731. https://doi.org/10.1029/2019JD031731.
6. Tripoli, G.J.; Cotton, W.R. Numerical Study of an Observed Orogenic Mesoscale Convective System. Part 1: Simulated Genesis and Comparison with Observations. *Mon. Weather Rev*. **1989**, *117*, 273–304.
7. Carbone, R.E.; Tuttle, J.D. Rainfall Occurrence in the U.S. Warm Season: The Diurnal Cycle. *J. Clim.* **2008**, *21*, 4132–4146. https://doi.org/10.1175/2008JCLI2275.1.
8. Kaplan, M.L.; Koch, S.E.; Lin, Y.-L.; Weglarz, R.P.; Rozumalski, R.A. Numerical Simulations of a Gravity Wave Event over CCOPE. Part I: The Role of Geostrophic Adjustment in Mesoscale Jetlet Formation. *Mon. Weather Rev.* **1997**, *125*, 1185–1211.
9. Zhang, F.; Koch, S.E. Numerical Simulations of a Gravity Wave Event over CCOPE. Part II: Waves Generated by an Orographic Density Current. *Mon. Weather Rev.* **2000**, *128*, 2777–2796.
10. Corbosiero, K.L.; Dickinson, M.J.; Bosart, L.F. The Contribution of Eastern North Pacific Tropical Cyclones to the Rainfall Climatology of the Southwest United States. *Mon. Weather Rev.* **2009**, *137*, 2415–2435. https://doi.org/10.1175/2009MWR2768.1.
11. Dominguez, C.; Magaña, V. The Role of Tropical Cyclones in Precipitation Over the Tropical and Subtropical North America. *Front. Earth Sci.* **2018**, *6*, 19. https://doi.org/10.3389/feart.2018.00019.
12. Ritchie, E.A.; Wood, K.M.; Gutzler, D.S.; White, S.R. The Influence of Eastern Pacific Tropical Cyclone Remnants on the Southwestern United States. *Mon. Weather Rev.* **2011**, *139*, 192–210. https://doi.org/10.1175/2010MWR3389.1.
13. Galarneau, T.J.; Bosart, L.F.; Schumacher, R.S. Predecessor Rain Events Ahead of Tropical Cyclones. *Mon. Weather Rev.* **2010**, *138*, 3272–3297. https://doi.org/10.1175/2010MWR3243.1.
14. Cote, M.R. Predecessor Rain Events in Advance of Tropical Cyclones. M.S. Thesis, University at Albany, State University of New York, Albany, NY, USA, 2007. Available online: https://vlab.noaa.gov/documents/2121416/4053968/Cote_Thesis.pdf/c70d8c89-7e16-5199-b15c-7450a9723273 (accessed on 10 December 2025).
15. ECMWF ERA5 Hourly Data on Pressure Levels from 1940 to Present. Available online: https://cds.climate.copernicus.eu/datasets/reanalysis-era5-pressure-levels?tab=documentation (accessed on 22 May 2025).
16. Skamarock, A.W.; Klemp, A.J.; Dudhia, A.J.; Gill, A.D.O.; Liu, A.Z.; Berner, A.J.; Wang, A.W.; Powers, A.J.G.; Duda, A.M.G.; Barker, A.D.; et al. *A Description of the Advanced Research WRF Model Version 4.1*; National Center for Atmospheric Research: Boulder, CO, USA, 2019.
17. *The NCAR Command Language*, (Version 6.6.2) [Software]; UCAR/NCAR/CISL/TDD: Boulder, CO, USA, 2019. http://doi.org/10.5065/D6WD3XH5.
18. PRISM/NACSE PRISM Group at Oregon State University. Available online: https://prism.oregonstate.edu/normals/ (accessed on 22 May 2025).
19. NOAA NCEI GIS Radar Data. Available online: https://www.ncei.noaa.gov/maps/ (accessed on 22 May 2025).
20. NOAA SPC Archive SPC Mesoscale Analysis (HTML5 JavaScript Version). Available online: https://origin-east-www-spc.woc.noaa.gov/exper/ma_archive/ (accessed on 22 May 2025).
21. Oolman, L. University of Wyoming Atmospheric Science Radiosonde Archive. Available online: https://weather.uwyo.edu/upperair/sounding.shtml (accessed on 22 May 2025).
22. Stein, A.F.; Draxler, R.R.; Rolph, G.D.; Stunder, B.J.B.; Cohen, M.D.; Ngan, F. NOAA's HYSPLIT Atmospheric Transport and Dispersion Modeling System. *Bull. Am. Meteorol. Soc.* **2015**, *96*, 2059–2077. https://doi.org/10.1175/BAMS-D-14-00110.1.